



# A coupled LBM-DEM method for simulating the multiphase fluid-solid interaction problem

Fei Jiang<sup>a,b,c,\*</sup>, Haihu Liu<sup>d</sup>, Xian Chen<sup>a</sup>, Takeshi Tsuji<sup>c,e</sup>

<sup>a</sup> Department of Mechanical Engineering, Yamaguchi University, Ube, Japan

<sup>b</sup> Blue energy center for SGE technology (BEST), Yamaguchi University, Ube, Japan

<sup>c</sup> International Institute for Carbon-Neutral Energy Research (WPI-I2CNER), Kyushu University, Fukuoka, Japan

<sup>d</sup> School of Energy and Power Engineering, Xi'an Jiaotong University, Xi'an, China

<sup>e</sup> Department of Earth Resources Engineering, Faculty of Engineering, Kyushu University, Fukuoka, Japan

## ARTICLE INFO

### Article history:

Received 27 October 2020

Received in revised form 2 November 2021

Accepted 5 January 2022

Available online 10 January 2022

### Keywords:

Gas-liquid-solid three-phase interaction

Lattice Boltzmann method

Discrete element method

Immersed boundary method

## ABSTRACT

In this paper, we develop a numerical model for simulating the solid-liquid-gas three-phase flow in unconsolidated particle layers. Based on the discrete element method (DEM) and the multiphase fluid model in the framework of the lattice Boltzmann method (LBM), a multiphase fluid-solid two-way coupling algorithm is proposed. In this model, the fluid-fluid interface is tracked using a phase-field method, and the multiphase fluid-particle interaction is tackled by a combination of the momentum exchange method for the flow field and the immersed boundary method for the phase field. We applied the method to simulate the upward migration of the leaked gas bubbles through a brine-filled sediment column at the seafloor, and investigated the influences of the leak flow rate and the interfacial tension on the bubble rising behavior. The results indicate three different flow regimes: connected finger flow, transition flow, and dispersed bubbly flow. These flow regimes can be distinguished by the dimensionless Eötvös and Weber numbers. The proposed numerical method can accurately characterize various multiphase interaction mechanisms at the mesoscopic scale and has powerful advantages in simulating complex fluid-particle coupling problems.

© 2022 Elsevier Inc. All rights reserved.

## 1. Introduction

The dynamic behavior of multiphase flows in a gas-solid-liquid mixture system plays an important role in various applications of petroleum industries, biochemical processing, chemical industry, metallurgical, food technology, water treatment, and sub-seabed CO<sub>2</sub> storage. Sub-seabed CO<sub>2</sub> storage is considered a promising solution for reducing carbon emissions and mitigating global warming. However, a risk of the sub-seabed CO<sub>2</sub> storage is leakage of the stored CO<sub>2</sub> due to unpredictable reasons such as earthquakes. For such a situation, understanding the hydrodynamics and the complex phase interactions of three-phase systems (gas, water and sediment) is important for considering the sedimentary structure formation during the escape of pore fluids (leaked gases) from loose, unconsolidated sediments. Furthermore, natural CO<sub>2</sub> and methane leakages are commonly observed in deep-sea environments, and such natural gas leakage is an important factor for carbon flux from

\* Corresponding author at: Department of Mechanical Engineering, Yamaguchi University, Ube, Japan.

E-mail address: fjiang@yamaguchi-u.ac.jp (F. Jiang).

the solid earth to the atmosphere [1]. To characterize such gas leakage (e.g., amount of gas leakage), we need to model the behavior of gas-solid-liquid mixture.

The strong coupling effect between fluids and sediment particles plays a vital role in determining not only the behavior of particle motions but also the flow patterns of the escaping fluids [2–4]. For example, if a pore space collapses, fluid will be forced to be squashed and flow out of the pore [5]. Numerical modeling of multiphase fluid-solid coupling would help reveal the mechanisms of the above phenomena. The multiphase computational fluid dynamics (CFD) based on conventional finite element (FE) or finite volume method (FVM) have been developed to simulate complex multiphase flows and their interactions with solid phase [6,7]. These multiphase CFD-particle coupled methods often used a coarse grid with simplification and cannot accurately characterize the flow around individual particles [8]. Direct numerical simulation (DNS) method [9,10] without assumptions is required to resolve the three-phase interactions between gas bubbles, rigid particles, and a Newtonian liquid at the scale of individual interfaces. Accurate tracking of sharp interfaces' evolution in DNS is particularly difficult because accurate calculations of surface tension force, momentum exchange between solid-fluid, and wettability are required. Li et al. [11] used a combined Euler-Lagrangian and DNS approach to investigate multi-bubble formation dynamics in gas-liquid-solid fluidization. However, it was pointed out that their model still needs assumptions for the particle-liquid interactions [10]. Ge and Fan [12] developed a combined Level-Set Immersed Boundary method (LS-IBM) to simulate gas-liquid-solid fluidized beds. Jain et al. [13] used a combined Volume-Of-Fluid Immersed Boundary method (VOF-IBM) to study the particle impact on thin liquid films and mimic wet particle collisions. Li et al. [14] proposed an immersed boundary-lattice Boltzmann method that simulates the multi-component fluid flows around moving solid boundaries. Chen et al. [15] developed a method to simulate particle motion in binary immiscible fluids using the link-based bounce-back model. However, particle-particle interaction has not been considered in these studies. Baltussen et al. [10] developed a hybrid front tracking immersed boundary model, which can simulate dense three-phase flows and accounts for the particle-particle interactions. They successfully simulated the bubble slurry columns by carefully considering the three-phase interactions. These conventional numerical methods, including finite element and finite volume-based method, usually need front-capturing and front-tracking methods such as volume-of-fluids (VOF), marker-and-cell (MAC), or level-set method to predict interface position and movement. The algorithms to characterize the interactions between fluid-fluid interface and fluid-solid interfaces are very complicated [12,16,11,13]. Besides, the three-dimensional simulation using such a conventional numerical method remains computation demanding, and treatments of such interfacial problems are usually very computationally expensive.

In addition to conventional numerical methods, the lattice Boltzmann method (LBM) has emerged as a powerful alternative tool for the solution of multiphase fluid flows. Unlike traditional CFD methods, which solve the conservation equations of macroscopic properties (i.e., mass, momentum, and energy) numerically, the basic idea of LBM is that it considers a many fictive particle system obeying the same conservation laws. Those particles perform consecutive propagation and collision processes over a discrete lattice mesh. LBM has several advantages in dealing with complex boundaries, incorporating microscopic interactions, flexible reproduction of interface between multiple phases, and parallelization of the algorithm. As most of the operations in LBM are local, LBM computation can be easily accelerated by using parallel computing technology [17]. Besides, it does not require complicated interface tracking algorithms as well as solving the implicit pressure equation. In addition, the surface tension and the contact angle required in DNS can be characterized from interaction forces between the particles of different fluids in LBM. These features make it an attractive tool for simulating complex flow behaviors, especially for modeling multiphase flows through porous media with complex geometries and large interface motion [18–21].

Regarding the characterization of granular media, the discrete element method (DEM) [22] is widely used to investigate the constitutive mechanical behavior of materials such as rock, soil, aggregates, and powders. In DEM, the granular system is modeled as an assemblage of geometrically simplified objects or elements (particles). The particle-particle interaction in DEM is evaluated through contact law. DEM has been successfully combined with traditional CFD schemes to simulate fluid-granular interaction behavior [23,24]. Recently, the coupling between LBM and DEM has been proposed for investigating various fluid-particle interacting problems, including the particle transport in flow [25–27], piping erosion [28], soil fluidization [29], multi-particle suspension simulation [30,31], and simulations of ascending fluid flow through granular deposits [32]. Since both the LBM and DEM are basically explicit, they are highly compatible from the computation and implementation points of view [25]. In these coupled DEM-LBM schemes, the interactions between fluid and solid particles are treated by the immersed boundary method [33,34] or the momentum exchange (ME) method [35,36] which can enforce a no-slip boundary condition between fluids and solids according to the conservation law of momentum. However, most of the above studies on LBM-DEM coupled methods are limited to single-phase flow. Coupling the multiphase LBM and DEM requires an algorithm to carefully deal with the co-evolution between the fluid-fluid interface and the fluid-solid interface because the two types of interfaces must not penetrate each other. Ding and Xu [37] proposed a multiphase fluid-solid coupling algorithm of LBM-DEM to simulate the debris flow with a free-surface model. However, such a free-surface model neglected the flow information of the gas phase. Kano et al. [38] developed a numerical method to simulate 3D solid-liquid-gas three-phase flow for investigating the leaked gas's behavior in the unconsolidated sandy seabed sediments. However, the mass conservation of each fluid phase cannot be ensured in their method. In this work, a novel DNS model will be presented for gas-liquid-solid three-phase flows by coupling the multiphase LBM and DEM with the considerations of mass conservation and the interactive interface dynamics.

This paper aims to develop a DNS method based on multiphase LBM-DEM coupling to investigate the solid-liquid-gas three-phase flow in the unconsolidated particle layers. Our method adopts an improved color-gradient model to solve the

immiscible multiphase flow [39,40]. This method has several advantages, such as the local mass conservation of each phase and the possibility of independently adjusting surface tension and viscosity ratio [41,42]. In this improved color-gradient model, the phase field is decoupled with the flow field and solved independently for the mass transport and the interface tracking in the lattice Boltzmann framework. The momentum transport of the bulk fluid are solved by LBM with a multiple-relaxation-time (MRT) collision operator [43]. The surface tension force and solid-fluid interaction force are considered as volumetric forces. The fluid-particle interaction is modeled by a combination of the momentum exchange method for the flow field and the immersed boundary method for the phase field. Finally, applications of the coupled model to the problem of bubbles seeping from unconsolidated particle layers are presented, and parameter studies were carried out to investigate the patterns of gas plume formation and particle motions by varying interfacial tension and leaking velocity.

## 2. Method

### 2.1. Governing equations

In our numerical model, we assume that both fluid phases are incompressible. The two fluids are integrated into a single set of governing equations. The mass and momentum conservation equations under an incompressible condition read

$$\nabla \cdot \mathbf{u} = 0, \quad (1)$$

$$\rho_f \left[ \frac{\partial \mathbf{u}}{\partial t} + (\mathbf{u} \cdot \nabla) \mathbf{u} \right] = -\nabla p + \mu_f \nabla^2 \mathbf{u} + \mathbf{F}, \quad (2)$$

where  $\rho_f$  and  $\mathbf{u}$  are the fluid's density and velocity;  $p$  and  $\mu_f$  denote the pressure and the dynamic viscosity. The body force  $\mathbf{F}$  is composed of gravity, surface tension force, and fluid-solid interaction force here. An order parameter  $\phi$  is utilized to characterize the configuration of binary fluid interface and identify two different fluids. The interface evolution is described by the advection equation of  $\phi$  based on the fluid velocity:

$$\frac{\partial \phi}{\partial t} + \mathbf{u} \cdot \nabla \phi = 0. \quad (3)$$

Across a flat interface,  $\phi$  changes from 1 to -1. With the order parameter, the viscosity at the interface transition area can be linearly interpolated:

$$\mu_f = \mu_g + \frac{\phi - \phi_g}{\phi_l - \phi_g} (\mu_l - \mu_g), \quad (4)$$

where the subscripts  $l$  and  $g$  indicate the two different fluids. The stress jump across the interface is given by [44]

$$\mathbf{T}_l \cdot \mathbf{n} - \mathbf{T}_g \cdot \mathbf{n} = -\nabla \cdot [\sigma (\mathbf{I} - \mathbf{n} \otimes \mathbf{n})] \quad (5)$$

where  $\mathbf{T} = -p\mathbf{I} + \mu_f (\nabla \mathbf{u} + \nabla \mathbf{u}^T)$  is the stress tensor,  $\mathbf{I}$  is the second-order identity tensor,  $\sigma$  is the interfacial tension, and  $\mathbf{n}$  is the interfacial unit normal vector.

The rigid particles immersed in fluid move individually based on Newton's laws. The translational and rotational motions of a particle are described as follows:

$$m_p \frac{d^2 \mathbf{x}_p}{dt^2} = \sum_{k=0}^{N_p} \mathbf{F}_k^c + \mathbf{F}_{hd}^{ext} + \mathbf{F}_{st}^{ext} + m_p \mathbf{g}, \quad (6)$$

$$\mathbf{I}_p \frac{d^2 \theta_p}{dt^2} = \sum_{k=0}^{N_p} \mathbf{T}^c + \mathbf{T}_{hd}^{ext} + \mathbf{T}_{st}^{ext}, \quad (7)$$

where  $m_p$  and  $\mathbf{I}_p$  are the mass and the moment of inertia of a particle, respectively;  $\mathbf{x}_p$ ,  $\theta_p$  denote the center position and the orientation of the particle.  $\mathbf{F}^c$  and  $\mathbf{T}^c$  are contact interaction forces and torques, which are calculated for each couple of particles;  $N_p$  is the number of adjacent particles in contact with current particle;  $\mathbf{g}$  is the gravitational acceleration.  $\mathbf{F}_{hd}^{ext}$  and  $\mathbf{T}_{hd}^{ext}$  are the external hydrodynamic load from the fluid domain.  $\mathbf{F}_{st}^{ext}$  and  $\mathbf{T}_{st}^{ext}$  are external load caused by the surface tension. The governing equations are solved with a coupled LBM-DEM method described below.

### 2.2. Numerical models

Coupling the multiphase LBM and DEM encounters difficulties because several interactions must be carefully modeled to produce the right physical behavior. These interactions include solid-solid interaction, fluid-fluid interaction (between two fluid phases), fluid-solid interactions (momentum exchange), and solid-fluid adhesion (wettability). The interface of two-phase fluid must not penetrate the moving solid boundary of DEM particles. In our method, the two-phase fluids are

considered immiscible, and dissolution was not assumed for simplicity. A phase-field model was adopted to characterize the fluid-fluid interaction, which is decoupled with the flow field and is only responsible for tracking the fluid-fluid interface evolution. The velocity field is calculated by a conventional MRT-LBM for the entire fluid domain with the consideration of interfacial tension forces. The interactions between the flow field and solid particle and the interactions between the phase field and particle are treated independently. The interpolated bounce-back scheme [45,46] was used to treat the interaction between the flow field and the particle, while the immersed boundary method [47] was adopted to handle the interaction between the phase field and the particle.

### 2.3. Numerical model for the velocity field

As a new alternative approach to solving the Navier-Stokes equations, we adopt the fully explicit LBM. The LBM is a mesoscopic kinetic-based approach that assumes the fluid flow is composed of a collection of pseudo-particles. These particles perform consecutive propagation and collision processes over a discrete lattice mesh. The particles' velocities are restricted to a finite set of vectors  $\mathbf{e}_i$ . A two-dimensional lattice with 9 velocity vectors (D2Q9 model) is used in the present study [48]. The velocity vectors are

$$\mathbf{e}_i = \begin{cases} (0, 0) & i = 0 \\ (\cos[(i-1)\pi/2], \sin[(i-1)\pi/2])c & i = 1-4 \\ (\cos[(2i-9)\pi/4], \sin[(2i-9)\pi/4])\sqrt{2}c & i = 5-8 \end{cases} \quad (8)$$

where lattice speed  $c = \Delta x / \Delta t$ ,  $\Delta x$  is the lattice length, and  $\Delta t$  is the constant time step. The weights for the D2Q9 stencil are

$$W_i^f = \begin{cases} 4/9, & i = 0 \\ 1/9, & i = 1-4 \\ 1/36, & i = 5-8 \end{cases} \quad (9)$$

The essential variable in the LBM is the particle distribution function (PDF)  $f_i(\mathbf{x}, t)$ , which represents the probability of encountering a particle with velocity  $\mathbf{e}_i$  and spatial position  $\mathbf{x}$  at time  $t$ . The fluid state is updated by calculating the particle distribution function  $f_i(\mathbf{x}, t)$  using the following discrete Boltzmann equation:

$$f_i(\mathbf{x} + \mathbf{e}_i \Delta t, t + \Delta t) = f_i(\mathbf{x}, t) + \Omega_i(f_i(\mathbf{x}, t)). \quad (10)$$

Under a low Mach number limit [49], Eq. (10) can be recovered to Eq. (2) by using the Chapman-Enskog expansion [50]. Here, the MRT collision operator is adopted:

$$\Omega = -\mathbf{M}^{-1} \mathbf{S} [\mathbf{M} \mathbf{f} - \mathbf{m}^{(eq)}]. \quad (11)$$

In the MRT model, the collision process is conducted in the momentum space.  $\mathbf{M}$  is the transformation matrix, which transforms the particle distributions into momentum space. We give a detailed description of the matrix  $\mathbf{M}$  in Appendix A. The moments of the distribution functions are expressed as

$$\mathbf{m} = (\rho, e, \varepsilon, j_x, q_x, j_y, q_y, p_{xx}, p_{xy})^T. \quad (12)$$

The physical meanings of these moments can be found in d'Humières et al. [51]. These moments are relaxed towards a local equilibrium with a diagonal matrix of relaxation coefficients  $\mathbf{S}$ . The diagonal matrix  $\mathbf{S}$  is given as follows:

$$\mathbf{S} = \text{diag}(0, s_e, s_\varepsilon, 0, s_q, 0, s_q, s_\nu, s_\nu). \quad (13)$$

The zero entries correspond to the conserved moments. Density  $\rho$  and momentums  $j_x, j_y$  are conserved values, that are not necessary to be relaxed. The relaxation rates  $s_\nu$  and  $s_e$  are associated with the kinematic viscosity  $\nu$  and bulk viscosity  $\zeta$  respectively:

$$\nu = c_s^2 \left( \frac{1}{s_\nu} - \frac{1}{2} \right) \Delta t, \quad \zeta = c_s^2 \left( \frac{1}{s_e} - \frac{1}{2} \right) \Delta t, \quad (14)$$

where  $c_s$  is the speed of sound, which is  $\frac{1}{\sqrt{3}} \frac{\Delta x}{\Delta t}$  for the D2Q9 lattice model. The other parameters  $s_\varepsilon, s_q, s_\pi$ , and  $s_m$  must be set within the range of [0,2] and can be tuned to improve their accuracy and stability [51]. The optimized values depend on the specific system's geometry and initial and boundary conditions. These optimal parameters are usually unknown in advance for general cases. In this study, we chose the 'magic' parameters that relax the even and odd moments with different values [52]. These parameters are set as:

$$s_e = s_\varepsilon = s_\nu, \quad s_q = \frac{8(2 - s_\nu)}{8 - s_\nu}. \quad (15)$$

The equilibria of the moments are given as follows:

$$\mathbf{m}^{(eq)} = \rho \left( 1, -2 + 3u^2, \alpha + \beta u^2, u_x, -u_x, u_y, -u_y, u_x^2 - u_y^2, u_x u_y \right)^T, \quad (16)$$

where  $\alpha = 1$  and  $\beta = -3$  to be consistent with BGK model [48].

The body forces acting on the fluid flow is imposed by the Guo's forcing schemes [53]. An extra forcing term is added into the right hand of Eq. (10):

$$\mathbf{G}_f = \Delta t \mathbf{M}^{-1} \hat{\mathbf{F}}, \quad (17)$$

where  $\hat{\mathbf{F}}$  denotes the moments of the forcing term in the moment spaces given as follows:

$$\hat{\mathbf{F}} = \begin{bmatrix} 0 \\ 6\left(1 - \frac{s_e}{2}\right) \mathbf{u} \cdot \mathbf{F} \\ -6\left(1 - \frac{s_e}{2}\right) \mathbf{u} \cdot \mathbf{F} \\ F_x \\ -\left(1 - \frac{s_q}{2}\right) F_x \\ F_y \\ -\left(1 - \frac{s_q}{2}\right) F_y \\ 2\left(1 - \frac{s_v}{2}\right) (u_x F_x - u_y F_y) \\ \left(1 - \frac{s_v}{2}\right) (u_x F_y + u_y F_x) \end{bmatrix}. \quad (18)$$

The macroscopic fluid density  $\rho(\mathbf{x}, t)$  and velocity  $\mathbf{u}(\mathbf{x}, t)$ , can be calculated from the following equations:

$$\rho_f = \sum_i f_i, \quad (19)$$

$$\rho_f \mathbf{u} = \sum_i \mathbf{e}_i f_i + \frac{\Delta t}{2} \mathbf{F}. \quad (20)$$

For the two-phase fluid system, the surface tension force  $\mathbf{F}_\sigma$  needs to be calculated to characterize the fluid-fluid interaction. Here, we adopted the continuum surface force (CSF) model [54] to calculate a volume force due to surface tension in the finite thickness transition region:

$$\mathbf{F}_\sigma(\mathbf{x}, t) = \frac{1}{2} \sigma \kappa \nabla \phi, \quad (21)$$

where  $\phi$  denotes the order parameter calculated from the phase field described in the next section. The curvature  $\kappa$  can be estimated from the gradient of phase field [55]:

$$\kappa = [(\mathbf{I} - \mathbf{n} \otimes \mathbf{n}) \cdot \nabla] \cdot \mathbf{n}, \quad (22)$$

where

$$\mathbf{n} = \frac{\nabla \phi}{|\nabla \phi|}. \quad (23)$$

The fluid-fluid interfacial tension force  $\mathbf{F}_\sigma$  is imposed using the forcing terms in Eq. (17). For the color-gradient multi-phase LBM, the fictitious-density (FD) model [56] is the most widely used wetting model because of its simplicity. In the FD model, the wetting tendency of the stationary solid surface can be controlled by setting a virtual order parameter  $\phi_w$  on the solid lattice nodes to a value from -1 (non-wetting/hydrophobic) to 1 (wetting/hydrophilic) or somewhere in between. This FD wetting model may cause spurious velocity near the interfaces [57]. The improved geometrical wetting models [55,58] can suppress the spurious velocity but require careful treatment to handle arbitrarily complex boundaries [59].

## 2.4. Numerical model for the phase field

The phase field can be described by the Cahn-Hilliard equation or the Allen-Cahn equation [60]. The lattice Boltzmann model based on the Cahn-Hilliard equation often encounters the mass conservation issue [61,62]. Small droplets may disappear when their radius is below a critical value [63]. Several modified models have been proposed to improve the mass conservation [64,65]. On the other hand, the lattice Boltzmann model based on the Allen-Cahn model usually suffers numerical errors, leading to the non-physical behavior of small droplets [66]. Since the phase field defined in this study is only

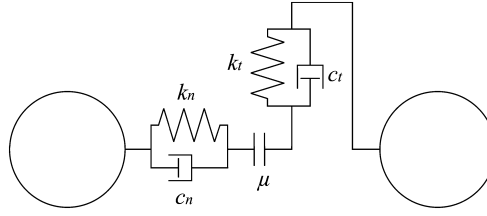


**Fig. 1.** Constitutive model of the contacting particles (Voigt model).

used for interface tracking, we solve Eq. (3) using two extra lattice Boltzmann equations (LBEs). The two extra LBEs only describe the mass transport behavior of the two fluid components based on the number density for each phase  $C^s$ , where superscript “s” indicates either fluid g or fluid l. The LBEs for the mass transport of two components are written as follows:

$$g_i^s(\mathbf{x} + \mathbf{e}_i \Delta t, t + \Delta t) = g_i^s(\mathbf{x}, t) - \frac{1}{\tau_g} \left[ g_i^s(\mathbf{x}, t) - g_i^{s(eq)}(\mathbf{x}, t) \right] + (1 - 0.5\tau_g) G_i^s(\mathbf{x}, t), \quad (24)$$

where  $g_i^{s(eq)}$  is the equilibrium populations,  $\tau_g$  is the single relaxation time, and  $G_i^s(\mathbf{x}, t)$  represents the source term in the lattice framework, which is used to impose the moving solid boundary condition in the phase field. In this study, we set  $\tau_g = 1.0$ , which enables an efficient implementation of LBEs for mass transport [67].

Here the equilibrium distribution  $g_i^{s(eq)}$  is given as follows:

$$g_i^{s(eq)} = W_i^f C^s \left( 1 + \frac{\mathbf{e}_i \cdot \mathbf{u}}{c_s^2} \right). \quad (25)$$

The same lattice model D2Q9 is used for the phase field. The number density of each phase  $C^s$  can be accordingly calculated as follows:

$$C^s = \sum_{i=1}^9 g_i^s. \quad (26)$$

The order parameter  $\phi$  can be defined from the number densities of the phase fields as follows:

$$\phi = \frac{C^l - C^g}{C^l + C^g}. \quad (27)$$

The color gradient  $\mathbf{C}_g$  is calculated in lattice framework as follows:

$$\mathbf{C}_g = \nabla \phi = \frac{3}{c^2 \Delta t} \sum_i W_i^f \mathbf{e}_i \phi(t, \mathbf{x} + \mathbf{e}_i \Delta t). \quad (28)$$

The  $\nabla \phi$  is related to the calculation of interface's orientation and is required for evaluating the surface tension (Eq. (21)). A recoloring algorithm is needed to cancel out the mass diffusion and keep the interface sharp for immiscible fluids. Here, we adopted the recoloring algorithm developed by Tolke et al. [39] which redistributes the mass distributions of  $C^g$  and  $C^l$  in a way that the inner product of the gradient  $\nabla \phi$  and the momentum of phase  $C^g$  is maximized. The implementation of this recoloring algorithm can be found in Appendix B. The velocity field and phase field are coupled together by inter-transferring the information of order parameter  $\phi$ 's spatial distribution and the information of advection velocity field  $\mathbf{u}$ .

## 2.5. Discrete element method

The DEM is based on the concept that individual objects are considered to be interact with each other along their boundaries by appropriate physical interaction laws. The particles are assumed to be rigid, but are allowed to overlap at the contact.

The contact forces can be obtained by a constitutive model [68], which is characterized by the normal and tangential stiffness  $k_n$  and  $k_t$ , respectively, the Coulomb friction coefficient  $\mu$ , and the normal and tangential contact damping coefficient  $c_n$  and  $c_t$  (Fig. 1). The rigid solid particles are allowed to slightly overlap with each other. The contact determination is carried out by calculating the distance  $L_{ij}$  between the particle centers:

$$L_{ij} \leq r_{pi} + r_{pj}, \quad (29)$$

$$L_{ij} = \sqrt{(x_{pi} - x_{pj})^2 + (y_{pi} - y_{pj})^2}, \quad (30)$$

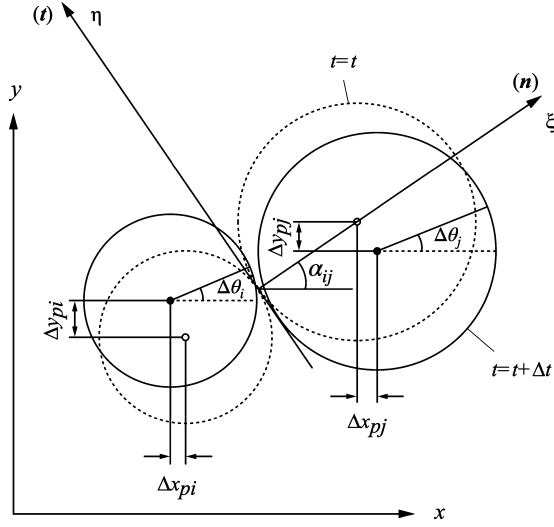


Fig. 2. Schematic of the local coordinate system and interparticle relative displacements.

where,  $r_p$  denotes the radius of particle,  $i, j$  are the indices of particles, and  $x_p, y_p$  represent the particle location in global coordinates. To calculate the contact force according to the constitutive model, we define a local coordinate system  $(\xi, \eta)$  with the contact point as the origin at time step  $t$ . The direction of  $\eta$ -axis is determined by the tangent vector of contacting point, while the  $\xi$ -axis is orthogonal to the tangent vector (Fig. 2). The relative displacement increments  $\Delta\xi_{ij}, \Delta\eta_{ij}$  in the local coordinate system can be calculated from the global displacements increments as follows:

$$\begin{bmatrix} \Delta\xi_{ij} \\ \Delta\eta_{ij} \end{bmatrix} = [T_{GL}] \begin{bmatrix} \Delta x_{pi} - \Delta x_{pj} \\ \Delta y_{pi} - \Delta y_{pj} \end{bmatrix} + \begin{bmatrix} 0 & 0 \\ \Delta\theta_i & \Delta\theta_j \end{bmatrix} \begin{bmatrix} r_{pi} \\ r_{pj} \end{bmatrix}, \quad (31)$$

where  $\Delta x_{pi}, \Delta y_{pi}, \Delta\phi_i$  are the increments of transitional and angular displacements respectively. The transform matrix  $T_{GL}$  is expressed by

$$[T_{GL}] = \begin{bmatrix} \cos\alpha_{ij} & \sin\alpha_{ij} \\ -\sin\alpha_{ij} & \cos\alpha_{ij} \end{bmatrix}, \quad (32)$$

$$\sin\alpha_{ij} = -\frac{y_{pi} - y_{pj}}{L_{ij}}, \cos\alpha_{ij} = -\frac{x_{pi} - x_{pj}}{L_{ij}}. \quad (33)$$

The first term on the right side of Eq. (31) represents the component due to translational displacement, and the second term represents the contribution from the tangential displacement caused by rotational motion.

Since the springs' forces and the dampers' forces are proportional to the relative displacement and the relative velocity in the constitutive model, the contact forces  $F_\xi$  and  $F_\eta$  in the local coordinate system can be expressed as

$$F_\xi(t) = e_n(t) + d_n(t), \quad (34)$$

$$e_n(t) = e_n(t - \Delta t) + k_n \Delta\xi_{ij}, \quad (35)$$

$$d_n(t) = c_n \frac{\Delta\xi_{ij}}{\Delta t}, \quad (36)$$

$$F_\eta(t) = e_t(t) + d_t(t), \quad (37)$$

$$e_t(t) = e_t(t - \Delta t) + k_t \Delta\eta_{ij}, \quad (38)$$

$$d_t(t) = c_t \frac{\Delta\eta_{ij}}{\Delta t}. \quad (39)$$

Here, we only take account of the compressive forces. Therefore, the interparticle forces are set to be zero when tensile normal forces occurred ( $e_n(t) < 0$ ). Considering the sliding, we used the simple tangential friction model to correct the tangential forces as follows:

$$F_\eta(t) = \mu \cdot \text{Sign}[e_n(t), e_t(t)], \text{ when } |e_t(t)| < \mu e_n(t). \quad (40)$$

The operator  $\text{Sign}[a, b]$  means adding the sign of  $b$  to the absolute value of  $a$ . Finally, interparticle forces and torque in the global coordinate system can be obtained by the following inverse transformation:



$$\begin{bmatrix} F_{pxi} \\ F_{pyi} \end{bmatrix} = - \sum_j [T_{GL}]_{ij}^{-1} \begin{bmatrix} F_{\xi} \\ F_{\eta} \end{bmatrix}_{ij}, \quad (41)$$

$$T_{pi} = -r_{pi} \sum_j [F_{\eta}]_{ij}. \quad (42)$$

After the interparticle force, capillary force and hydrodynamic forces are all obtained, the motion equation of particle (Eq. (6) and (7)) can be solved with the time integration method for calculating the particle displacement during time  $\Delta t$ .

### 2.5.1. Time integration of DEM

The DEM usually uses an explicit time integration scheme [69]. Many explicit integration schemes have been developed, e.g. Euler integration, leapfrog integration [70], velocity Verlet integration [71], Gear's Predictor-Corrector [72] and Runge-Kutta [73]. Here we adopted the velocity Verlet integration method, which is a second-order time integration scheme originally developed in the context of structural dynamics. It also has several attractive properties. First, it is symplectic and time reversible; second, only terms differing one order in  $\Delta t$  at maximum are combined; third, it is easy and efficient to be implemented. The detailed time integration scheme for the translational motion is implemented as follows:

$$\mathbf{a}_{pi}(t) = \frac{\mathbf{F}_i^{total}(t)}{m_{pi}}, \quad (43)$$

$$\mathbf{v}_{pi}(t + \frac{1}{2}\Delta t) = \mathbf{v}_{pi}(t) + \frac{1}{2}\mathbf{a}_{pi}(t)\Delta t, \quad (44)$$

$$\mathbf{x}_{pi}(t + \Delta t) = \mathbf{x}_{pi}(t) + \mathbf{v}_{pi}(t + \frac{1}{2}\Delta t)\Delta t, \quad (45)$$

where, the  $\mathbf{v}_{pi}$  and  $\mathbf{a}_{pi}$  denote the  $i$ th particle's acceleration and velocity, respectively;  $\mathbf{F}_i^{total}(t)$  denotes the total forces acting on  $i$ th particle. Finally, we can update the velocity at the next time step by:

$$\mathbf{v}_{pi}(t + \Delta t) = \mathbf{v}_{pi}(t + \frac{1}{2}\Delta t) + \frac{1}{2}\mathbf{a}_{pi}(t + \Delta t)\Delta t. \quad (46)$$

The integration scheme for rotational motion is implemented with the similar manner.

## 2.6. Coupling between multiphase LBM and DEM

### 2.6.1. Interaction between flow field and moving particles

The interactions between flow field and moving particles are treated by the interpolated bounce-back (IBB) schemes [45,46]. Compared with the conventional half-way bounce-back scheme, which is first-order accurate for moving boundary, the IBB achieves a second-order accuracy [74–76]. In Fig. 3, the solid boundary of a particle is represented by the red curve. Coordinates of fluid node  $\mathbf{x}_f$  and internal solid node  $\mathbf{x}_b$  are determined by judging the relative position of particle's boundary and fluid's lattice grids. The wall nodes  $\mathbf{x}_w$  are located at the intersection points on the solid boundary along the bouncing back directions. After the collision step, the PDF at  $\mathbf{x}_b$  which need to be streamed back to the fluid node is unknown. In IBB, this unknown PDF  $f_i^-(\mathbf{x}_b, t)$  is estimated by performing a linear interpolation of the populations located at the neighbor fluid nodes  $\mathbf{x}_f$  and  $\mathbf{x}_{ff}$  as follows:

$$f_i^-(\mathbf{x}_b, t) = 2\eta f_i^+(\mathbf{x}_f, t) + (1 - 2\eta) f_i^+(\mathbf{x}_{ff}, t) + \frac{6}{c^2} \rho_f W_i^f \mathbf{u}_w \cdot \mathbf{e}_i, \quad \eta < 0.5 \quad (47)$$

$$f_i^-(\mathbf{x}_b, t) = \frac{1}{2\eta} f_i^+(\mathbf{x}_f, t) + \frac{2\eta - 1}{2\eta} f_i^+(\mathbf{x}_{ff}, t) + \frac{3}{\eta c^2} \rho_f W_i^f \mathbf{u}_w \cdot \mathbf{e}_i, \quad \eta \geq 0.5 \quad (48)$$

where the “+” denotes post-collision, and  $\bar{i}$  denotes the opposite direction of  $i$ :  $\mathbf{e}_{\bar{i}} = -\mathbf{e}_i$ . The  $\mathbf{u}_w$  represents the wall node's velocity obtained from the particle motions in DEM, which can be calculated from the particle's transitional and angular velocities ( $\mathbf{v}_p$  and  $\omega_p$ ) by:

$$\mathbf{u}_w = \mathbf{v}_p + \omega_p \mathbf{r}_c, \quad (49)$$

$$\mathbf{r}_c = \mathbf{x}_w - \mathbf{x}_c, \quad (50)$$

where  $\mathbf{x}_c$  denotes the coordinates of particle center. In Eq. (47) and (48),  $\eta$  is the fraction of intersected link calculated as:

$$\eta = |\mathbf{x}_f - \mathbf{x}_w| / |\mathbf{x}_f - \mathbf{x}_b|. \quad (51)$$

For the moving boundary condition, the initialization (refilling technique) of the fresh nodes that emerged from the solid phase is important to achieve high accuracy because it dramatically affects the oscillation of the force evaluation [76]. In this study, we adopted the non-equilibrium extrapolation scheme for the refilling scheme [77] as:



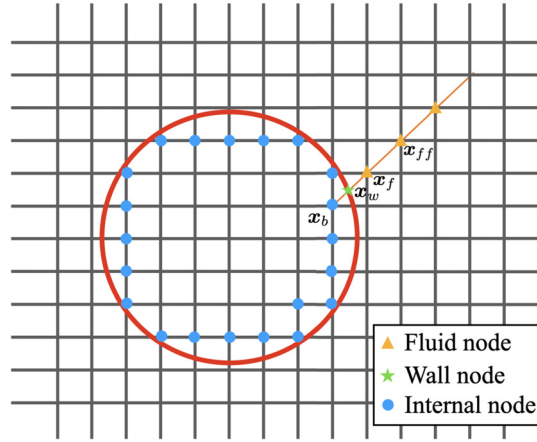


**Fig. 3.** A sketch of a fluid-solid interface with different types of boundary nodes in IBB scheme. (For interpretation of the colors in the figure(s), the reader is referred to the web version of this article.)

$$f_i(\mathbf{x}, t + \Delta t) = f_i^{eq}(\rho_f^{\text{average}}, \mathbf{u}_w) + f_i(\mathbf{x} + \mathbf{e}_i \Delta t, t + \Delta t) - f_i^{eq}(\mathbf{x} + \mathbf{e}_i \Delta t, t + \Delta t), \quad (52)$$

where  $\rho_f^{\text{average}}$  denotes the averaged density of original surrounding fluid nodes. The PDF of a new fluid node is calculated as a sum of an equilibrium part and the non-equilibrium distribution function directly from the neighboring fluid nodes. A second-order extrapolation method [76] for the refilling can be used to improve the force oscillation. However, it is reported that the improved refilling technique has almost no effect on the velocities and trajectories of the particles [76]. Due to the particle movement, some fluid nodes may become inactive when the particles cover them. The PDFs of these new inactive nodes are disregarded [78,79]. Note that the refilling scheme cannot exactly conserve mass for the momentum equation due to the extrapolation treatment.

The force acting on the wall nodes of a DEM particle can be calculated using a modified Galilean invariant momentum exchange method as:

$$\mathbf{F}_i(\mathbf{x}_w) = (\mathbf{e}_i - \mathbf{u}_w) f_i^+(\mathbf{x}_f, t) - (\mathbf{e}_i - \mathbf{u}_w) f_i^+(\mathbf{x}_b, t). \quad (53)$$

The total hydrodynamic force  $\mathbf{F}_{hd}^{ext}$  and torque  $\mathbf{T}_{hd}^{ext}$  in Eq. (6) and Eq. (7) acting on the particle can be evaluated by summing the forces of all the wall nodes of the particle based on the momentum exchange as:

$$\mathbf{F}_{hd}^{ext} = \sum_j \sum_i \mathbf{F}_i(\mathbf{x}_{w,j}), \quad (54)$$

$$\mathbf{T}_{hd}^{ext} = \sum_j \sum_i (\mathbf{x}_{w,j} - \mathbf{x}_c) \times \mathbf{F}_i(\mathbf{x}_{w,j}). \quad (55)$$

Instead of the momentum exchange method, the stress integration method [80] can be alternatively adopted to improve the accuracy of the force evaluation in the low spatial resolution conditions [76]. The performance of the momentum exchange method is sufficient if the resolution is fine enough [76].

### 2.6.2. Interaction between phase field and moving particles

The interactions between the phase field and moving particles were treated using the immersed boundary concept to maintain the mass conservation of each phase. The traditional interpolated bounce-back scheme that treats the moving boundary condition for the flow field cannot be directly applied to the phase field because the associate refilling process violates the mass conservation. The second difficulty in the multiphase fluid-particle simulations is to properly treat both the evolution of fluid-fluid interfaces and the movement of solid-fluid interfaces. This difficulty arises because the fluid-fluid interface is modeled by the diffuse-interface approach, while the solid-fluid interface is always sharp. Preventing the diffuse fluid-fluid interface from penetrating the moving particle's sharp boundary is important to accurately characterize the proper behavior of rising bubbles in sediment. Baltussen et al. [10] developed a gas-fluid-particle simulation method by using a front tracking method with a set of marker points to model a sharp fluid-fluid interface. However, their method is not volume conservative and the intersection of the two types of interfaces may occur. To solve this problem, we introduce an extra term that mimics a non-flux solid boundary condition to prevent the penetration of the fluid-fluid interface. A zero flux correction method combined with an immersed boundary scheme [47] is adopted to treat the moving particles' boundary in the phase field. In this method, the moving sharp solid boundary is treated inside the diffuse phase field using the concept of IBM, and a correcting source term is calculated to cancel off the mass flux into the solid boundary. In IBM, the moving particles' boundary is represented by  $N$  points [81], and the boundary Lagrangian points  $\mathbf{X}_k$  generally differ

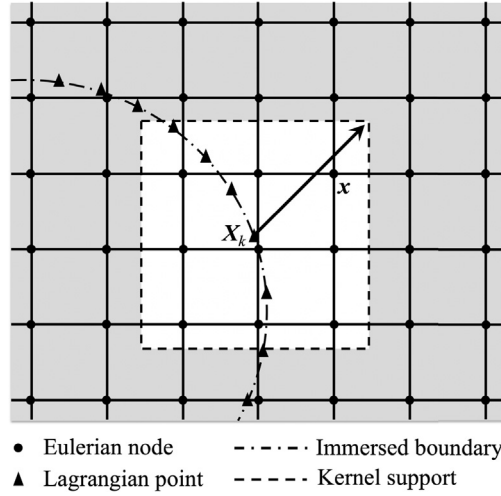


Fig. 4. Solid boundary represented by a set of Lagrangian points immersed in the fluid domain.

from the background Eulerian grids  $\mathbf{x}$  of the fluid (Fig. 4). The source terms  $G^S(\mathbf{x}, t)$  in Eq. (24) are applied on the Eulerian grids near the Lagrangian points on the interface to satisfy the nonpenetration condition.

Like the conventional IBM, the present approach proceeds in two main steps: interpolation of mass flux vector and distribution of source/sink term. Supposing that the current  $g_i(\mathbf{x}, t)$ ,  $\mathbf{u}(\mathbf{x}, t)$ , and  $C^S(\mathbf{x}, t)$  are known, the temporary  $g_i^*(\mathbf{x}, t + \Delta t)$  can be estimated by Eq. (24) without the source term, and the temporary flux vector can be calculated as follows:

$$\mathbf{h}^*(\mathbf{x}, t + \Delta t) = \sum_{i=1}^9 g_i^*(\mathbf{x}, t + \Delta t) [\mathbf{c}_i - \mathbf{u}(\mathbf{x}, t + \Delta t)]. \quad (56)$$

The flux vector  $\mathbf{h}^*(\mathbf{X}_k, t + \Delta t)$  at the boundary Lagrangian points can be then interpolated as follows:

$$\mathbf{h}^*(\mathbf{X}_k, t + \Delta t) = \sum_{\mathbf{x}} \mathbf{h}^*(\mathbf{x}, t + \Delta t) W(\mathbf{x} - \mathbf{X}_k) (\Delta x)^2, \quad (57)$$

where,  $\sum_{\mathbf{x}}$  denotes the summation over all lattice nodes  $\mathbf{x}$  and the  $W$  is a weighting function proposed by Peskin [82] as follows:

$$W(x, y) = \frac{1}{\Delta x} w\left(\frac{x}{\Delta x}\right) \cdot \frac{1}{\Delta y} w\left(\frac{y}{\Delta y}\right). \quad (58)$$

The  $w(r)$  is a mollifier to the Dirac delta function, which is equal to zero out of the kernel support (Fig. 4):

$$w(r) = \begin{cases} \frac{1}{8} \left( 3 - 2|r| + \sqrt{1 + 4|r| - 4r^2} \right) & |r| \leq 1 \\ \frac{1}{8} \left( 5 - 2|r| - \sqrt{-7 + 12|r| - 4r^2} \right) & 1 < |r| \leq 2 \\ 0 & \text{otherwise} \end{cases} \quad (59)$$

To implement the desired zero-flux condition at the Lagrangian points  $\mathbf{X}_k$  in its normal direction, a source term  $q(\mathbf{X}_k, t + \Delta t)$  is determined by [47]:

$$q(\mathbf{X}_k, t + \Delta t) = -2 \frac{\mathbf{n}_k(t + \Delta t) \cdot \mathbf{h}^*(\mathbf{X}_k, t + \Delta t)}{\Delta x}, \quad (60)$$

where  $\mathbf{n}_k(t + \Delta t)$  is the unit normal vectors of the boundary at the Lagrangian points  $\mathbf{X}_k$ . Finally, the source terms  $q(\mathbf{X}_k, t + \Delta t)$  are distributed to the lattice points by:

$$q(\mathbf{x}, t + \Delta t) = \sum_{k=1}^N q(\mathbf{X}_k, t + \Delta t) W(\mathbf{x} - \mathbf{X}_k) \Delta V, \quad (61)$$

where  $\Delta V$  is the control volume calculated as  $S/N \times \Delta x$  with  $S$  being the perimeter of the circular particle. The source term in Eq. (24) can be calculated from the macroscopic flux as:

$$G_i^S(\mathbf{x}, t + \Delta t) = \Delta x W_i^f q(\mathbf{x}, t + \Delta t). \quad (62)$$

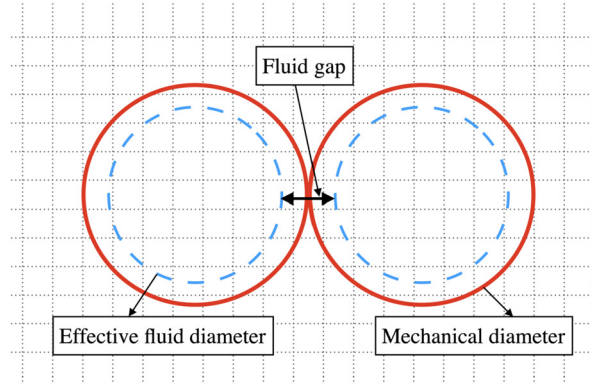


Fig. 5. Schematic of effective fluid diameter; squares depict lattice mesh.

To ensure the mass conservation, we scale the total sources produced from a particle to equal the internal mass that was diffused into the particle. The scaling factor is determined by the ratio of internal mass to the total sources from the boundary nodes. For the traditional bounce-back scheme, a similar correction term can be used to improve the mass conservation [2]. Finally, the  $g_i^s(\mathbf{x}, t + \Delta t)$  and  $C^s(\mathbf{x}, t + \Delta t)$  can be updated by Eq. (24) and Eq. (26). Note that the present method (zero-flux scheme) can only treat the perfect wetting condition for the solid particles due to incompatibility between the solid's sharp boundary and the fluid-fluid's diffuse interface in the IBM framework. The internal solid nodes are filled with the wetting fluid and the order parameters  $\phi$  on the solid boundary nodes are directly obtained from the wetting fluid density field, whose value is ideally 1.0. In this manner, the perfect wetting condition is automatically achieved according to the FD wetting model. It is reported that the FD wetting model has a large spurious velocity [57]. However, when the viscosity of non-wetting phase is high, the spurious currents can be suppressed [55]. Moreover, if the perfect wetting condition is considered, the fluid-fluid interface has a minimum contact area with the solid boundary. Therefore, the impact of spurious velocity on the force evaluation for the particle is insignificant.

To counter the impact of the phase field on the particles, we must consider the capillary force due to the surface tension separately because it cannot be introduced by the implementation of the momentum exchange method [83]. Since we focus on the perfect wetting scenario and the particle is immersed in the wetting fluid, the capillary force exerted on the Lagrangian point  $\mathbf{X}_k$  is approximately calculated by an interpolation from the surface tension force field  $\mathbf{F}_\sigma(\mathbf{x}, t)$  as follows:

$$\mathbf{F}_\sigma(\mathbf{X}_k, t) = \sum_{\mathbf{x}} \mathbf{F}_\sigma(\mathbf{x}, t) W(\mathbf{x} - \mathbf{X}_k) (\Delta x)^2. \quad (63)$$

Finally, the external load due to surface tension in Eq. (6) and (7) can be estimated as follows:

$$\mathbf{F}_{st}^{ext} = - \sum_k \mathbf{F}_\sigma(\mathbf{X}_k), \quad (64)$$

$$\mathbf{T}_{st}^{ext} = - \sum_k (\mathbf{X}_k - \mathbf{x}_c) \times \mathbf{F}_\sigma(\mathbf{X}_k). \quad (65)$$

Note that the above-mentioned approximate estimation of capillary force is only available for the perfect wetting condition. To accurately calculate the capillary force, we can use an alternative way in the framework of the momentum exchange method [83].

### 2.6.3. Effective hydraulic diameter

In our two-dimensional model, we may encounter the situation that there are no connected paths for fluid to flow with the circumstance of densely packed sediments, while in a 3D granular assembly, the pore space between grains is interconnected. Therefore an assumption about the flow paths needs to be made to facilitate the applicability of two-dimensional simulation [5]. This situation also brings difficulties in treating the moving boundary conditions of IBB. When two particles are in contact with each other, linear extrapolation may access the inside solid domain of the other particle. This problem results in not only a decrease in accuracy but also the instability of the simulations. Here, we use a similar approach by Boutt et al. [5], introducing an effective hydraulic diameter (dashed line in Fig. 5) for the computation of fluid and fluid-solid interaction. The effective hydraulic diameter is approximated by a reduction in the mechanical particle diameter  $d$ . Therefore, a fluid gap  $d_f$  between two particles in contact is estimated as follows:

$$d_f = 2d(1 - d_h), \quad (66)$$

where  $d_h$  is a reduction percentage for the effective hydraulic diameter. Note that the original mechanical diameter is used for computing the particle-particle interactions. Therefore, both the normal and shear forces provided by the contact

between the discrete elements and the hydraulic forces from fluid momentum calculations based on the resulting fluid gap will be involved in computing the movement of particles. Since discrete elements are allowed to overlap a small amount in DEM, reducing effective hydraulic diameter is inevitable when overlap occurs. In this study, we set reduction percentage  $d_h$  to be a small constant value of 15%.

When particles are very close to contact, there is another issue that lubrication force becomes important because of the formation of boundary lubrication films. Such an effect becomes dominant when the inertia of particles is small [84]. Such lubrication films are very thin and are usually unable to be resolved when the moving particles are close enough (no fluid sites in the interstice). The effective hydraulic diameter also enables us to add back the unresolved part to recover the correct lubricating behavior to some extent with appropriate calibration [85].

#### 2.6.4. Subcycling time integration

There are two time steps used in our method,  $\Delta t$  for the fluid flow and  $\Delta t_{DE}$  for the particles. The LBM time step is determined by  $\Delta t = (\tau - \frac{1}{2}) \frac{(\Delta x)^2}{3\nu}$ . Generally, the critical time step  $\Delta t_{DE}^{cr}$  for DEM is determined according to the period of oscillation for a single mass-spring system as  $2\sqrt{m_p/k_n}$ . To ensure the simulation stability of multiple-particle systems, the time step of integration should be even smaller:  $\Delta t_{DE} \leq \alpha_t \Delta t_{DE}^{cr}$ , where  $\alpha_t$  is a parameter that accounts for the presence of multiple contacts for a particle. Here, we chose  $\alpha_t = 0.1$ , which is recommended by Hart et al. [86]. Yang et al. [27] mentioned that the presence of fluid helps to damp the low-frequency elastic waves and increase the stability of DEM which allows a larger value of  $\Delta t_{DE}$ . However, our numerical test shows that the  $\Delta t_{DE}$  still needs to be smaller than the  $\Delta t_{DE}^{cr}$ . When the time step  $\Delta t$  of LBM is larger than  $\Delta t_{DE}$ , a subcycling time integration is necessary to ensure the correspondence between the two physical time steps. The  $\Delta t_{DE}$  is reduced to a new value  $\Delta t_{DE}^n$ , so that the ratio between  $\Delta t$  and  $\Delta t_{DE}^n$  is an integer  $N_{sub}$ :

$$\Delta t_{DE}^n = \frac{\Delta t}{N_{sub}} (N_{sub} = \lceil \Delta t / \Delta t_{DE} \rceil + 1), \quad (67)$$

where  $\lceil \cdot \rceil$  denotes an integer round-off operator. Therefore, in one step of the fluid computation,  $n$  sub-steps of time integration are performed for the DEM part with  $\Delta t_{DE}^n$ . During the subcycling, the hydrodynamic forces are assumed to be unchanged [25]. Our numerical tests showed that the numerical stability is good when subcycling number  $N_{sub}$  is below 60. On the other hand, the  $\Delta t_{DE}$  can simply be forced to equal the time step of LBM when  $\Delta t_{DE} > \Delta t$ . To avoid the situation that the particle passes through the fluid-fluid interface, the particle should not move more than grid length during one time step  $\Delta t$  of LBM. Therefore, the maximum particle velocity must be lower than the lattice speed:  $U_p^{max} < \Delta x / \Delta t$ .

#### 2.6.5. Coupling algorithm

The flowchart of the coupling algorithm between multiphase LBM and DEM is presented in Fig. 6. First, the information of the flow field, phase field and the particles are initialized. Unless otherwise stated, the distribution functions of  $f_i$  and  $g_i$  are initialized as the equilibria with the initial values of density and velocity. The flow field is firstly evolved according to the boundary condition of the fluid domain considering momentum transfer between the particle and fluid (particle-fluid interaction forces). Note that the surface tension forces are also calculated from the phase field at this moment and included in the body force term. The phase fields of the two fluids are advected using the bulk fluid's velocity distributions at the same time with the consideration of source term calculated from the particle boundaries. The anti-diffusion recoloring process is exerted for the phase field to prevent mixing and keep the interface sharp. The hydrodynamic forces and torques acting on the particles are then calculated and applied. If the sub-cycling algorithm is adopted,  $N_{sub}$  DEM sub-cycles are performed for each time step of LBM evolution to synchronize the particle and flow motions. With the hydrodynamic forces and particle-particle contacting forces, the information of particle motions in terms of accelerations, velocities and positions are calculated and updated. Based on the new particle position, the lattice cells covered by the solid particles are re-identified and the refilling process is conducted for the emerged fluid-type lattices. The coordinates of the Lagrangian points are updated for the immersed boundary scheme to calculate the flux boundary condition for the phase field. Finally, all the macroscopic properties can be updated to the next time step.

### 2.7. Validations

#### 2.7.1. Droplet in contact with a cylinder

We first validate the wetting boundary conditions on curved surfaces by placing a droplet on top of a circular cylinder without considering gravity. The cylinder is fixed in this validation case. Therefore, the simple bounce-back scheme instead of IBM is used here to treat the solid boundary condition for phase field, and the FD model is adopted to impose the wetting condition. The droplet deforms until the prescribed contact angle  $\theta$  is reached (Fig. 7). At equilibrium, an arc with radius  $r$  will be formed on the top of the cylinder with a radius  $R_s$ . From the geometrical characteristics in Fig. 7, we can calculate the area of the droplet in terms of its radius  $r$  and the distance  $k(r, \theta)$  between the center of the droplet and the center of the circular cylinder by the following equation [58]:

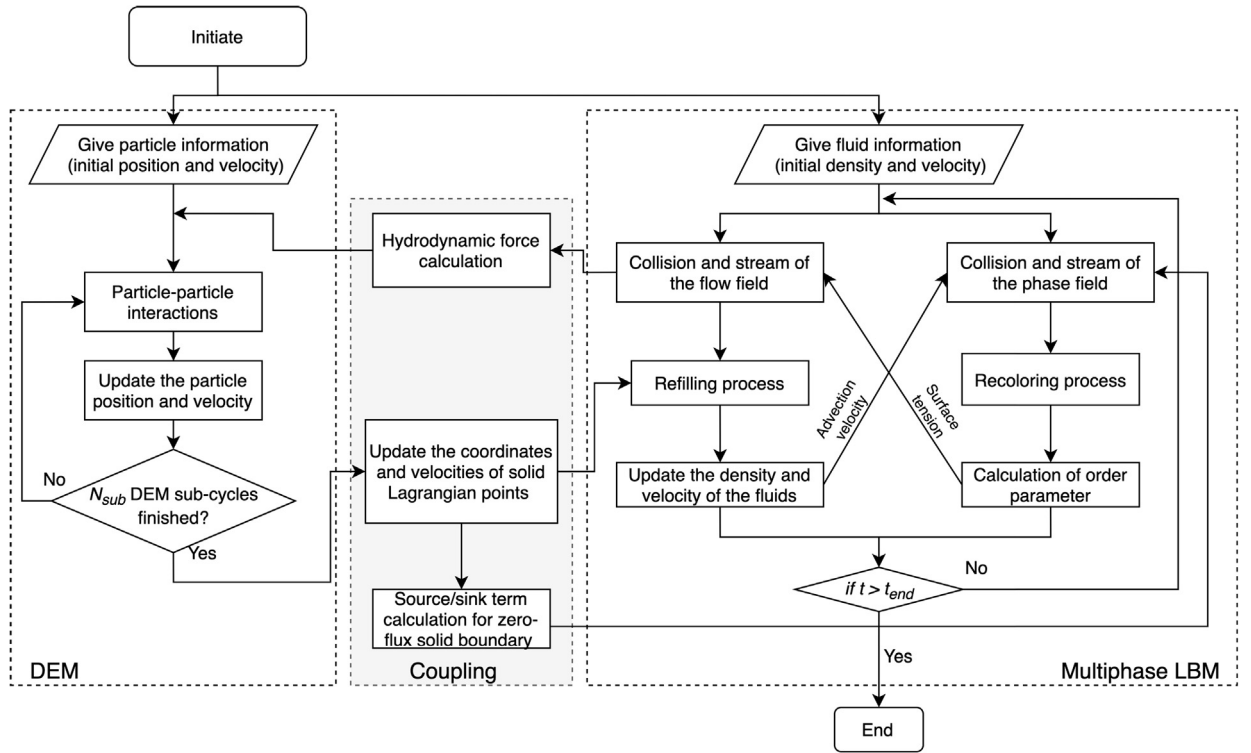
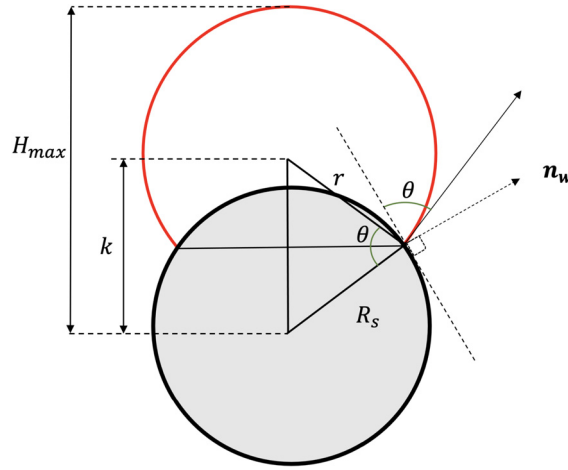


Fig. 6. Flowchart of the multiphase LBM-DEM coupling scheme.

Fig. 7. A schematic of the shape of the droplet resting on the circular cylinder with radius  $R_s$ .

$$A(r, k) = \pi r^2 - r^2 \cos^{-1} \left( \frac{k^2 + r^2 - R_s^2}{2kr} \right) - R_s^2 \cos^{-1} \left( \frac{k^2 - r^2 + R_s^2}{2kR_s} \right) + k \sqrt{R_s^2 - \left( \frac{k^2 - r^2 + R_s^2}{2k} \right)^2} \quad (68)$$

where,  $k$  is

$$k(r, \theta) = \sqrt{r^2 + R_s^2 - 2rR_s \cos \theta} \quad (69)$$

In the simulation, the cylinder is centered at  $(L_0/2, L_0/4)$  in a square domain whose length is  $L_0$ . A droplet with radius  $R = R_s = L_0/6$  is initially placed at  $(L_0/2, L_0/4 + R_s)$ . The computational domain of size  $L_0 \times L_0$  is resolved with  $128 \times 128$  grid points. The surface tension  $\sigma$  is chosen to be 0.01, and the viscosities of both fluids are identical ( $\mu_l = \mu_g = 0.1$ ). The periodic boundary condition is used in the horizontal direction, and the halfway bounce-back scheme is applied at the top and bottom walls to obtain the no-slip condition. We set the contact angle ranging from  $45^\circ \leq \theta \leq 135^\circ$ . For each case, the

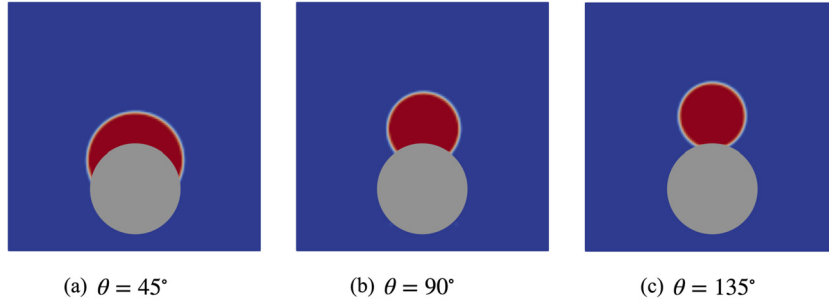


**Fig. 8.** Equilibrium shape of a droplet on a cylindrical surface for three different contact angles: (a)  $\theta = 45^\circ$ , (b)  $\theta = 90^\circ$  and (c)  $\theta = 135^\circ$ . The red color represents the droplet, while the gray region represents the cylinder.

**Table 1**

The LBM simulation parameters for different grid resolutions.

Grid resolution	$\rho$	$\sigma$	$\nu$	$\Delta x$ (m)	$\Delta t$ (s)	$M_0$ (kg)
$32 \times 32$	1.0	0.0025	0.025	$8 \times 10^{-6}$	$4 \times 10^{-7}$	$6.4 \times 10^{-14}$
$64 \times 64$	1.0	0.005	0.05	$4 \times 10^{-6}$	$2 \times 10^{-7}$	$8 \times 10^{-15}$
$128 \times 128$	1.0	0.01	0.1	$2 \times 10^{-6}$	$1 \times 10^{-7}$	$1 \times 10^{-15}$
$256 \times 256$	1.0	0.02	0.2	$1 \times 10^{-6}$	$0.5 \times 10^{-7}$	$1.25 \times 10^{-16}$

simulation is run until the steady state is reached. Fig. 8 shows the results of the equilibrium shape of the droplet for three different contact angles. These results show a qualitative agreement with the prescribed contact angles.

To quantitatively evaluate our results, we measured the distance  $H_{max}$  between the top of the droplet and the center of the cylinder from our simulation results. Because the initial area of the droplet is  $(\frac{\pi}{3} + \frac{\sqrt{3}}{2})R_s^2$  in our simulation, the analytical solution of the droplet's radius  $r$  at equilibrium state can be determined by equating Eq. (68) with the initial area if the contact angle is known. Finally, the analytical result of  $H_{max}$  can be obtained from the droplet's radius  $r$  and distance  $k$  [58]. We also examine the grid independence of the results on four different grid resolutions with  $L_0 = 32, 64, 128$ , and 256. Because our simulations were conducted in lattice space, the physical value of density, interfacial tension and viscosity can be obtained using the following relationship [87]:

$$\rho^{phy} = \rho^{LBM} \frac{M_0}{\Delta x^3}, \sigma^{phy} = \sigma^{LBM} \frac{M_0}{\Delta t^2}, \eta^{phy} = \eta^{LBM} \frac{M_0}{\Delta x \Delta t} \quad (70)$$

where  $M_0$  is the mass scale. When we use different grid and time resolutions, the mass scale and LBM simulation parameters must be adjusted according to the above relationships (Eq. (70)). For example we choose  $\Delta x = 2 \times 10^{-6}$  m,  $\Delta t = 10^{-7}$  s and  $M_0 = 1 \times 10^{-15}$  kg for the case with the grid resolution  $128 \times 128$ . Note that we refine both space and time resolution by keeping  $\Delta x/\Delta t$  as a constant. The LBM simulation parameters for different resolutions are listed in Table 1. As can be seen in Fig. 9, there is a large discrepancy between the analytical results and the simulation results with low resolution ( $32 \times 32$  grid). The difference in droplet shape cannot be resolved when the change of contact angle is small. If we increase the number of grid points from  $32 \times 32$  to  $64 \times 64$ , a smoother relationship between contact angle and  $H_{max}$  is obtained, and the numerical results approach to the analytical solution (Fig. 9). However, there is a noticeable discrepancy between the analytical results and the simulation results, especially for the cases with low contact angles. On the other hand, the simulation results with grids  $128 \times 128$  and  $256 \times 256$  are indistinguishable and show good agreement with the analytical results (Fig. 9), which indicates that the present model can offer an accurate prediction of static contact angles on curved solid surfaces.

Fig. 10 plots the time variations of density at the droplet center with different grid resolutions. It can be seen that there is an overshoot of density in the low-resolution case ( $32 \times 32$  grid). The density converged to a constant value after the peak. However, the converged value of density deviates from the unity due to the weakly-compressible error [43] if the resolution is low. On the other hand, density slightly fluctuates around the unity in the cases with high resolutions ( $64 \times 64, 128 \times 128$  and  $256 \times 256$  grids) at the initial stage. Finally, density converged close to unity when the equilibrium state is reached. At equilibrium state, the difference in terms of density variations between the case with grid  $128 \times 128$  and the case with grid  $256 \times 256$  is trivial. To further analyze the accuracy of our method, we also compute the relative L1 error for  $H_{max}$ . It can be seen that our method has a first-order convergence rate (Fig. 11). Note that the validation of the non-perfect wetting conditions by using the FD model only works for the conventional bounce-back method in the phase field.

### 2.7.2. Droplet falling on a circular cylinder

We then simulated the process of a droplet falling on a circular cylinder and compared our results with the reference data [58]. The computational setup is illustrated in Fig. 12. The computational domain size is  $L_0 \times 2L_0$ , where  $L_0 = 128$ . A stationary cylinder with a radius  $R_s = L_0/10$  is located at the center ( $L_0/2, L_0$ ) of the domain. The initial position of

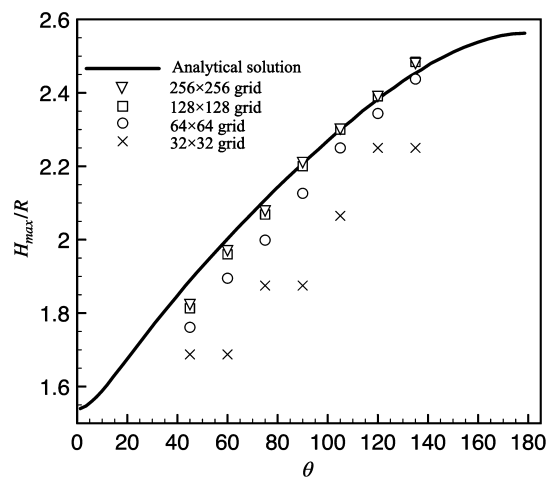


Fig. 9. Comparison between the analytical solution and numerical results with different grid sizes.

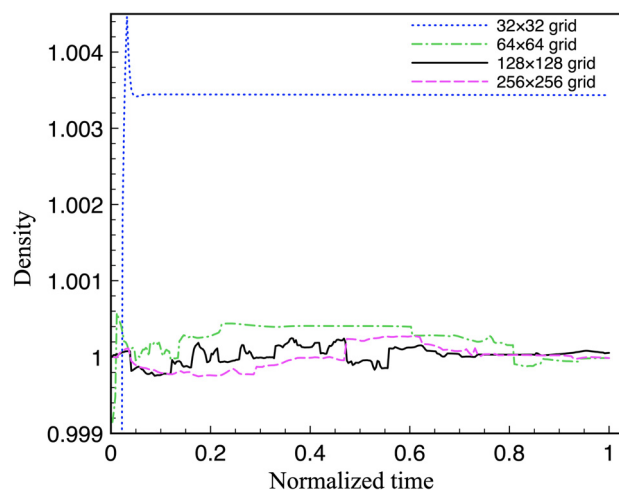


Fig. 10. Time variations of density at the droplet center with different grid resolutions.

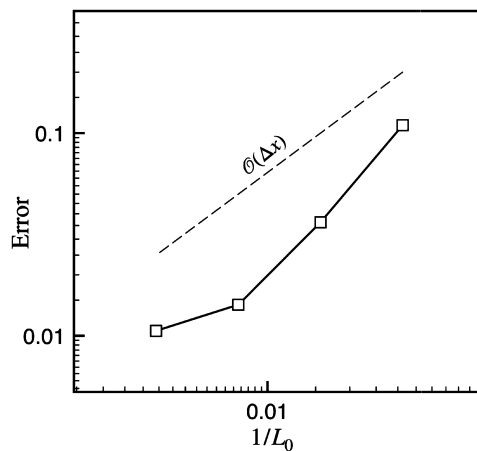
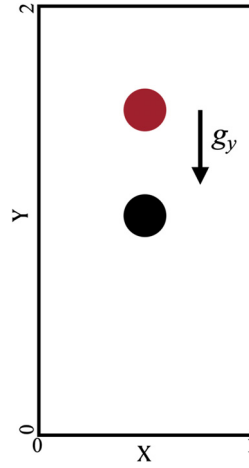
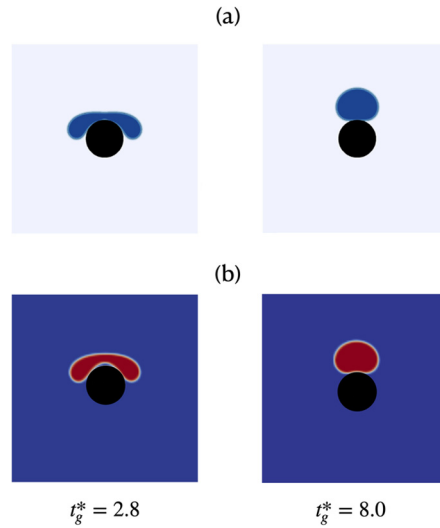


Fig. 11. Relative L1 error for the results of  $H_{max}$ . The dashed line indicates the first-order convergence rate.





**Fig. 12.** Computational domain for a droplet falling on a cylindrical surface.



**Fig. 13.** Droplet impact on a superhydrophobic cylinder with  $Re_{Gr} = 25$  and  $Bo = 2.2$ : (a) reference data [58]; (b) our numerical results.

the droplet with  $R_d = R_s$  is located at  $(L_0/2, 3L_0/2)$ . No-slip bounce-back condition is applied at the top and bottom wall, and periodic conditions are used in the  $x$ -direction. A body force  $g_y$  is applied on the droplet region, and the droplet will accelerate from rest and impact the cylinder.

Here, two dimensionless numbers are used to characterize the problem: gravity Reynolds number  $Re_{Gr} = \rho \sqrt{g_y D^3} / \mu$  and Bond number  $Bo = g_y \Delta \rho D^2 / \sigma$ , where  $D$  denotes the diameter of the droplet. We considered that the cylinder has a superhydrophobic surface. Here, we set the properties of the fluids such that  $Re_{Gr} = 25$  to match the cases of the reference literature [58] for comparison. Two cases with different Bond numbers ( $Bo = 2.2$  and  $3.3$ ) were considered here. The dimensionless time is defined as  $t_g^* = t \sqrt{g_y / D}$ . For the low Bond number case (Fig. 13), the droplet first deformed and retracted after hitting the cylindrical surface. The gravitational force failed to overcome surface tension force, and the droplet finally settled down on the cylinder. For the high Bond number case (Fig. 14), the surface tension plays a less important role, and the droplet broke up into two small sub droplets when impacting on the upper part of the cylinder. The two sub droplets were repelled from the cylindrical surface because of the superhydrophobicity and completely detached from the cylinder. The results of both cases showed a good agreement with the reference data [58] regarding both the droplet deformation and motion (Fig. 13 and 14).

### 2.7.3. Bubbles percolating through particle-rich suspensions

We then reproduce the behavior of bubbles percolating through a layer of particles suspended in a viscous fluid [88] to evaluate the performance of our method for resolving three-phase interactions. In Belien et al.'s experiment [88], a randomly packed layer of plastic cubes was suspended in corn syrup and the gas migration through the suspension layer was observed (Fig. 15). To mimic the experiment [88], we set a computational domain of 25 cm wide and 25 cm tall. This

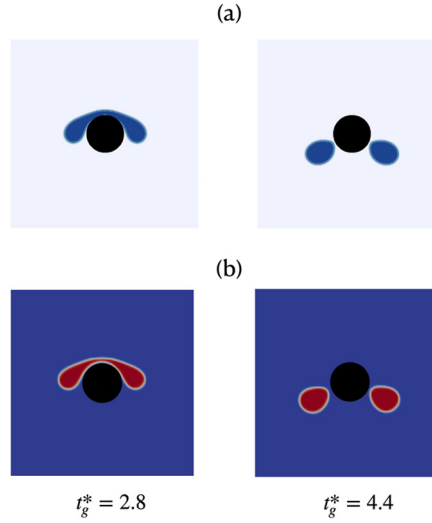


**Fig. 14.** Droplet impact on a superhydrophobic cylinder with  $Re_{Cr} = 25$  and  $Bo = 3.3$ : (a) reference data [58]; (b) our numerical results.

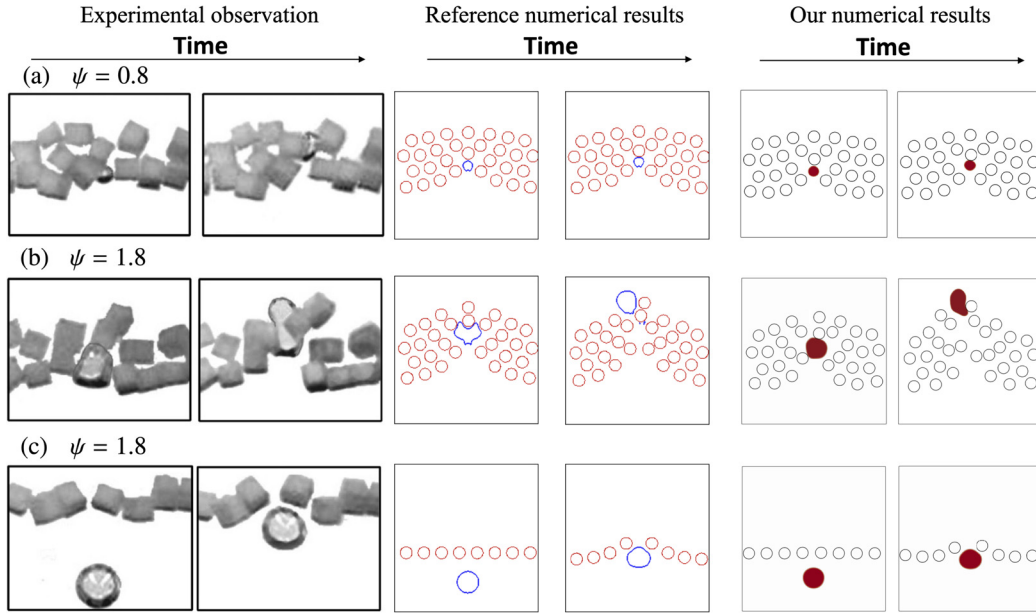


**Fig. 15.** Interaction between a rising bubble and suspended rigid particles.  $\psi$  represents the ratio of bubble size to particle size. Simulated interaction modes (right column) with bubble size and layer thicknesses are in agreement with experiment observation (left column) [88] and reference numerical results (middle column) [9].

domain is divided into a  $400 \times 400$  square lattice for the simulation. The interfacial tension and viscosity of the syrup were  $0.071 \text{ N/m}$  and  $4.12 \text{ Pa}\cdot\text{s}$  [88], respectively. No-slip bounce-back conditions are applied at the top and bottom walls, and periodic conditions are used in the horizontal direction. We used circular instead of square particles in the experiment in order to compare the present results with other numerical results [9]. Initially, the particles with identical size (a radius of  $9.7 \text{ mm}$ ) were uniformly distributed and suspended in corn syrup. The density of the solid particle is set to be  $1320 \text{ kg/m}^3$  [88]. The liquid phase preferentially wets the solid particles. The rising behavior of bubbles with different volumes was simulated.

Fig. 15 shows the different behavior of multiphase interactions between particles and bubbles with different bubble sizes and layer thicknesses. The ratio  $\psi$  between bubble size and particle size plays an important role in determining the interaction mode [88]. If the bubble is small, it rises through the pores with minimal deformation and is hard to displace the particles (Fig. 15 (a)). On the other hand, large bubbles largely deform and are able to displace the particles and create a pathway through the layer (Fig. 15 (b) and (c)). It can be seen that our simulation results are in good agreement (Fig. 15) with both the experiment observation [88] and reference numerical results based on the finite difference method [9].

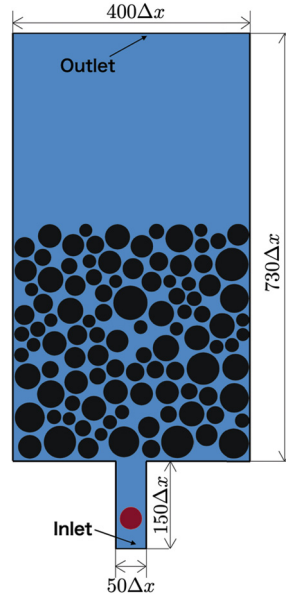


Fig. 16. Schematic of the computational system for simulating leaked gas bubble through a brine-filled sediment column.

### 3. Results and discussion

We applied our method to investigate the upward migration of leaked gas bubble through a brine-filled sediment column at the seafloor. A channel can be formed among sand grains in the unconsolidated sandy sediment layer due to the leakage. This process can be simplified as bubbles seeping from the unconsolidated particle layer, which is simulated by our developed solid-liquid-gas three-phase flow solver. In our simulation, two assumptions have been made: the sand particles were spherical and the gas does not dissolve into water. The influences of the leaking channel's velocity, interfacial tension, and consolidating state of particles on the bubble rising behavior and its plume formation were studied.

#### 3.1. Computational domain and conditions

Fig. 16 shows the schematic view of the present computational domains. The fluid domain is divided into a  $400 \times 880$  square lattice with spacing  $\Delta x = 1.25 \times 10^{-4}$  m. A vertical channel with the size of  $50\Delta x \times 150\Delta x$  is created at the bottom domain as the leakage opening of the bubbles. A halfway bounce-back scheme is used to apply the no-slip boundary conditions at the left and right solid walls. A parabolic velocity profile is imposed at the inlet of the flow channel:

$$v_f^y(0, x) = 1.5\bar{U} \frac{x(H-x)}{(0.5H)^2}, \quad v_f^x(0, x) = 0, \quad (71)$$

where  $\bar{U} = 0.05$  m/s is the spatially mean inlet velocity, and  $H$  is channel width. This velocity boundary condition is imposed by the scheme of Zou & He [89]. The corresponding 2D flow rate is  $q_r = H\bar{U}$ . For the outlet, a constant pressure boundary condition is imposed using Guo's non-equilibrium extrapolation scheme [90]. Note that the density ratio of the fluids is set to unity because of the limitation of the color-gradient model used in our method [91]. A body force which is equal to  $\Delta\rho gV$  is applied on the bubble with a volume  $V$  to mimic the combined effects of the gravity and buoyant force. The physical lattice spacing and time step in LBM were chosen to be  $\Delta x = 1.25 \times 10^{-4}$  m and  $\Delta t = 2.6 \times 10^{-5}$  s, respectively. A total of 105 circular particles with different sizes uniformly distributed from 2.5 to 7.5 mm are first randomly placed at the bottom area of the domain. The initial static state of the sediment layer (see in Fig. 16) is then obtained by updating the position of these particles using the free fall packing algorithm. The distance between the adjacent Lagrangian points on the particle boundary used in IBM is set to be the same with the Eulerian lattice spacing. The initial bubble size is set to be  $20\Delta x$  in radius, and the leak frequency of the bubble is  $3.85 \text{ s}^{-1}$ . The kinematic viscosities of both fluid phases are set to be  $1.0 \times 10^{-5} \text{ m}^2/\text{s}$ , and the following parameters for DEM are chosen [38]: particle density  $\rho_s = 5000 \text{ kg/m}^3$ , contact stiffness  $k_n = k_s = 5 \times 10^6 \text{ N/m}$ , contact damping ratio = 0.5. The time step of DEM is  $\Delta t_{DE} = 5.2 \times 10^{-7} \text{ s}$  for the motion simulation of the particles.

#### 3.2. Influence of interfacial tension: consolidated vs. unconsolidated

The rising behavior of the bubble in particle layers is influenced by many physical properties, e.g., the opening diameter, initial leakage bubble size, the flow rate, the confining pressure, and the interfacial tension (IFT). For small bubbles, the

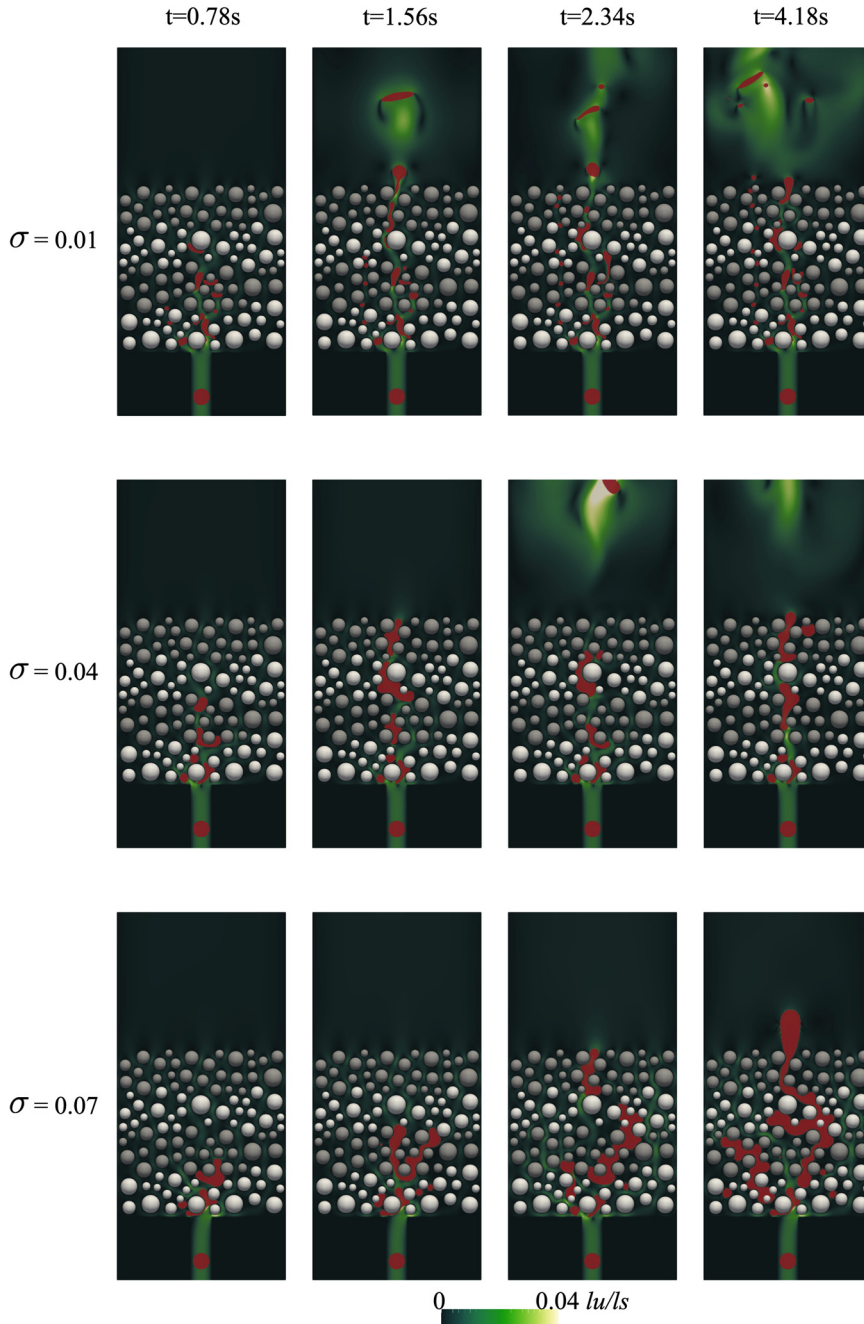


**Fig. 17.** The rising behavior of bubbles in consolidated sediment with different interfacial tensions. The red color represents the gas bubble phase, and the color bar indicates the magnitude of flow velocity. The original layers of the particles are illustrated with different colors: white and grey.

effects of IFT can be significant to determine the bubble dynamics. For stability issues, the value of surface tension must satisfy  $\sigma < \frac{\rho_f \Delta x^3}{2\pi \Delta t^2}$  with a given spatial and temporal resolution [23]. Here, we adjusted the IFT ranged from 0.01 to 0.07 in lattice units and studied its influence on the rising behavior of bubbles and channel formation due to the leaked gas in the unconsolidated sandy sediment layer. In addition, the consolidated system was also simulated by applying a sufficiently large confining pressure to the particle layers for comparison, i.e., the particles were assumed to be fixed. For the unconsolidated seabed sediment, the confining pressure can be negligible [38]. Fig. 17 and 18 show the rising behavior of leaked gas bubbles under different IFT conditions in the consolidated sediment and unconsolidated sediment, respectively. It can be seen that the increased IFT (largely undeformable) can cause the formation of the connected gas plume structure and partial bubble trapping (bubble stalls when trying to pass through the particle layer) in the consolidated case (Fig. 17). Meanwhile,

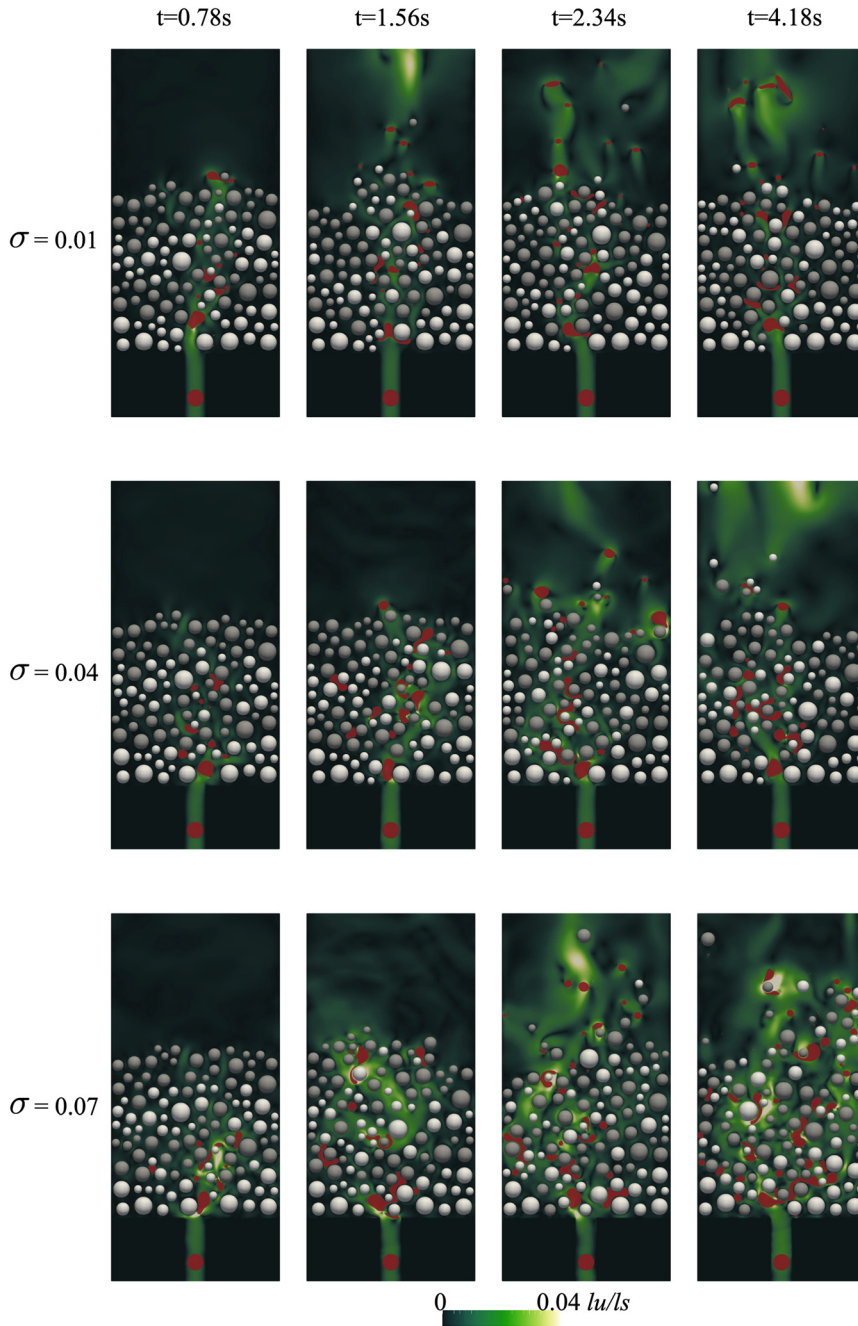


**Fig. 18.** The rising behavior of bubbles in unconsolidated sediment with different interfacial tensions. The red color represents the gas bubble phase, and the color bar indicates the magnitude of flow velocity. The original layers of the particles are illustrated with different colors: white and grey.

the bubbles were split into smaller ones due to the particle motion and could not be trapped even under the high IFT condition in the unconsolidated case (Fig. 18). The rising velocity through the particle layer of the unconsolidated case is much faster than that for the consolidated case (Fig. 17 and 18). Higher rising speed results in a shorter time for the bubble to pass through the particle layers. The effects of IFT on the breakthrough time (Fig. 19) and bubble sizes (Fig. 20) were further investigated.

The breakthrough time was measured as the time cost from initial leakage to the state that bubbles migrated to the top surface of the particle layer and entered into the pure water region. The breakthrough times for different IFT conditions are presented in Fig. 19. For the consolidated case, higher IFT leads to a longer time for the bubble passing through the grain region. Bubbles are easily trapped in the pore spaces at the high IFT condition because high surface tension force prohibits surface stretching. Moreover, the bubble coalescence frequently occurs, forming a large volume of bubbles (Fig. 20). On the



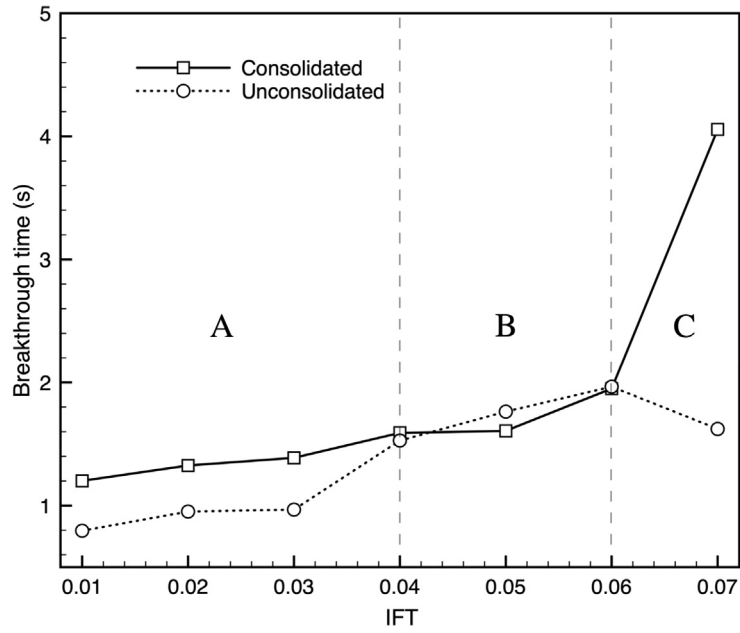


Fig. 19. Breakthrough time with different IFT conditions for consolidated and unconsolidated system.

other hand, the bubble easily breaks up and can pass through narrow pore spaces when IFT is low. For the unconsolidated case, the bubble cannot be trapped regardless of the IFT value because the pore space changes due to particles' movement and it is difficult to form a stable flow path. Therefore, the IFT has only a limited influence on the breakthrough time for the unconsolidated case. There is even a slight decrease of breakthrough time for the highest IFT case (Fig. 19). Comparing the results of consolidated and unconsolidated cases, we can observe that the bubble reaches the top surface of grains faster under the unconsolidated condition in general. Three regions can be distinguished: region A (low IFT), region B (medium IFT), and region C (high IFT) (Fig. 19). In region A, the breakthrough time is slightly longer for the consolidated case because the fixed grains act as the obstacle for the bubble to pass through, and the flow path is more tortuous. The breakthrough times are comparable in region B for the consolidated and unconsolidated circumstances. In this region, increased IFT results in a wider spread of bubbles and an unstable condition caused by the dominant capillary forces [92] for the unconsolidated case (Fig. 18). However, for the consolidated case, the bubbles straightly pass through the grain layer. Therefore, the extra rising time caused by the bubble spreading in the unconsolidated case becomes comparable with the delay due to the fixed obstacle grain in the consolidated case. In region C, the breakthrough time of the consolidated case increased rapidly with the increase of IFT due to the large volume of the trapped bubble, and it is almost 2.5 times longer than that of the unconsolidated case. On the other hand, the breakthrough time does not increase with the increase of IFT for the unconsolidated case in Region C, because no trapping occurs when the grains are moveable. The boards of these regions may shift for different leaking velocity conditions because of the changed balance between injected kinetic energy and interfacial energy.

The volume of bubbles passed through the grain layer greatly impacts both the latter rising behavior and dissolution behavior in the water column. The average bubble size under different IFT conditions was calculated by detecting the region of individual bubbles from the binarized phase field. The bubble size increased fast with the increase of IFT for the consolidated case (Fig. 20). The surface of the bubble becomes difficult to be stretched when the IFT is high. The bubble is easy to be trapped in the fixed pore spaces. Moreover, coalescence occurs, forming a large volume of bubbles that can be stable under high IFT condition. On the other hand, the bubble size kept a small level even if we increase the IFT for the unconsolidated case. It is clearly observed that the bubbles failed to be trapped in pore space if the grain is mobile (Fig. 18). The instability induced by the high IFT leads to the high kinetic energy of grains, which becomes possible to push the bubbles deforming and breaking-up even when the surface tension force is large. The small bubbles under the unconsolidated condition will accelerate the dissolution process after passing through the grain layer.

### 3.3. Influence of interfacial tension to particles' kinetic energy

Focusing on the unconsolidated system, we calculated the time-averaged total kinetic energy of all the particles (Fig. 21) under different IFT conditions. The kinetic energy of grains increased with the increase of IFT. It can be observed that the original layers of particles were totally destroyed under the high IFT condition (Fig. 18). The leaked bubble with low IFT tends to split into small ones when hitting the grains at the early stage. On the other hand, high IFT leads to a situation where the bubble becomes difficult to deform, and large bubbles temporarily block the flow paths inducing instability.

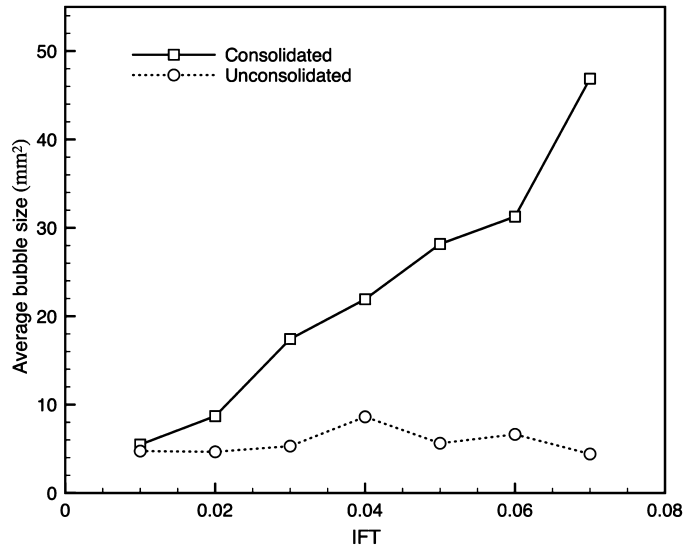


Fig. 20. Average bubble size under different IFT conditions for consolidated and unconsolidated system.

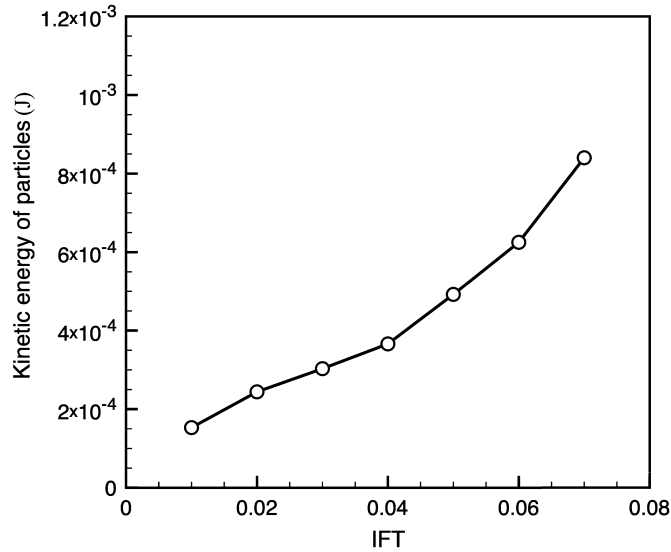


Fig. 21. Total kinetic energy of grains under different IFT conditions.

Fewer flow paths cause high flow velocity and high momentum exchange between fluid and grains. Therefore, the higher hydrodynamic forces acting on the grains cause the fast displacement of grains under high IFT conditions. Such displacement of surrounding grains and their inertia further lead to the instability of the particle system, which eventually breaks the trapped bubble and eliminates the formation of stable flow paths. Besides, capillary forces acting on grains are larger for the high IFT cases, which also accelerate the particle's motion. As a result, the particles move faster at high IFT conditions.

### 3.4. Influence of leak channel's flow velocity

The effect of the leak channel's flow velocity was further investigated by adjusting the mean velocity  $\bar{U}$  in Eq. (71) while fixing the value of IFT to 0.02. Here, we simulated three additional cases with various mean velocities:  $\bar{U} = 0.005$  m/s, 0.025 m/s, and 0.1 m/s. When the leaking velocity is low, the buoyancy force dominates and the leaked bubble forms a stable single finger-like stream (Fig. 22). Most of the grains kept their original location, meaning that the hydrodynamic forces were too small compared to the gravity forces. On the other hand, the high leak velocity created an open path for the bubble to travel through at the very early stage. Besides, high leaking velocity introduces considerable kinetic energy to the grains system through the fluid-solid interaction. The grains' kinetic energy obviously increased as the leak velocity increases (Fig. 23) due to the increasing fluid's momentum. The high kinetic energy of grains leads to the destruction of the original layer structures of the grain stack in high-velocity conditions (Fig. 22).



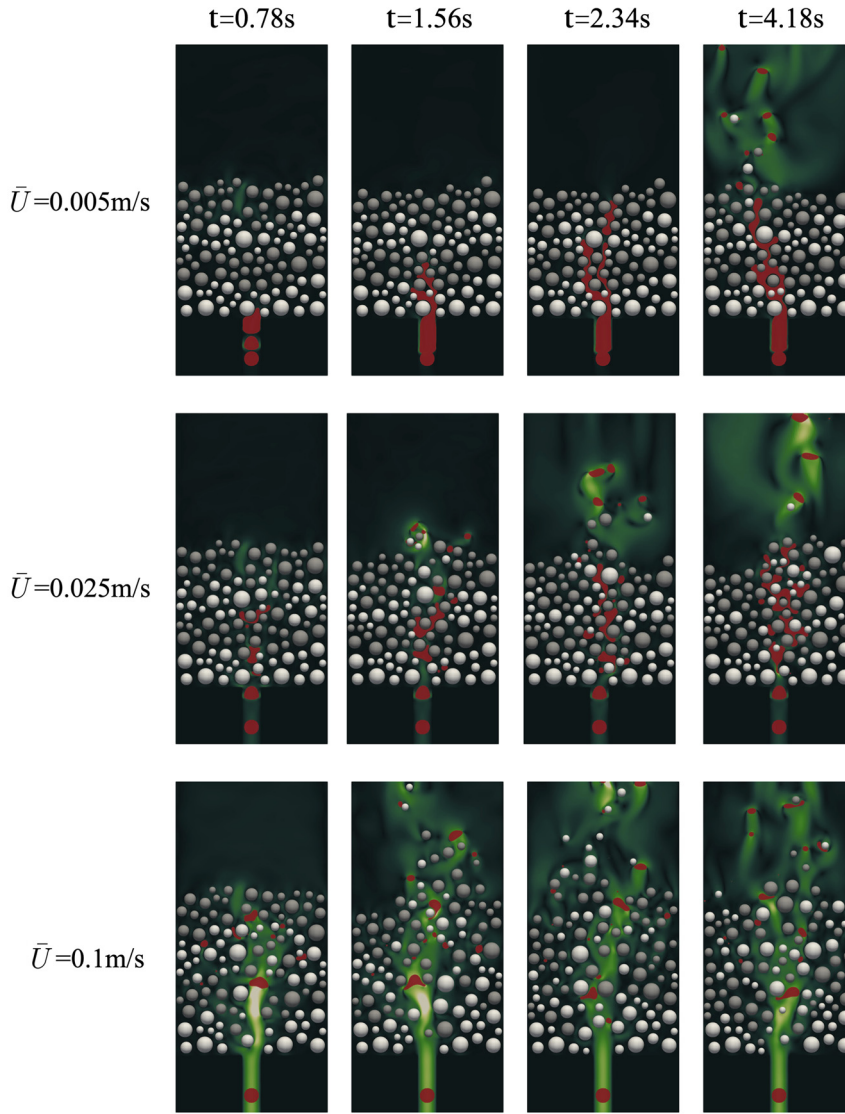


**Fig. 22.** Effect of the leak channel's flow velocity on the rising behavior of bubbles. The red color represents the gas bubble phase, and the color bar indicates the magnitude of flow velocity. The original layers of the particles are illustrated with different colors: white and grey.

The individual bubble's volume significantly decreased with the initial increase of leak flow velocity and finally approached towards a converged value (Fig. 23). In low leak velocity conditions, the leak bubbles merged into a large volume because the bubbles are able to be trapped when grains hardly move. On the other hand, high kinetic energy in the high leak velocity condition leads to severe impact between the grains and bubbles, and the leaked gas breaks up into smaller bubbles. The averaged bubbles' size remains almost unchanged (Fig. 23) after increasing the leak velocity over a certain threshold value (around 0.05 m/s).

### 3.5. Flow regimes of rising bubbles in sediment

The behavior of the gas bubbles rising in porous media can be characterized by the two dimensionless numbers: Eötvös number and Weber number [93,94]. The Eötvös number (EO) is the ratio of gravitational forces to surface tension forces, which is defined as follows:

$$EO = \frac{\Delta\rho g V}{\sigma L}, \quad (72)$$

where  $L$  is the length of the fluid-fluid interface, and  $V$  is the total volume of the gas phase. The Weber number (WE) is a measurement of the relative importance of the fluid's inertia compared to its surface tension, which is defined as follows:

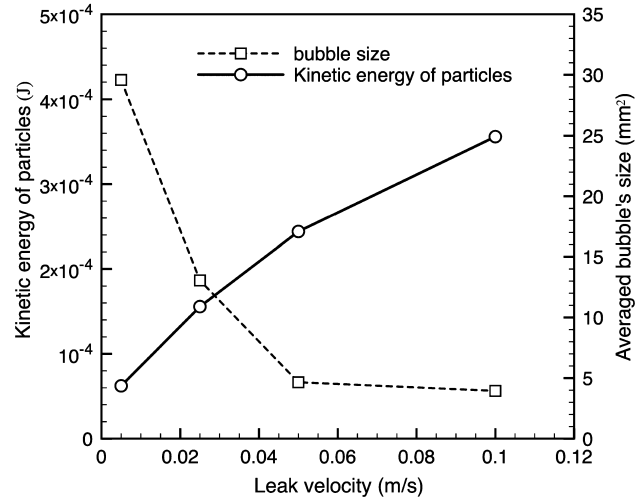


Fig. 23. Effect of the leak channel's flow velocity on particles' kinetic energy and bubble sizes.

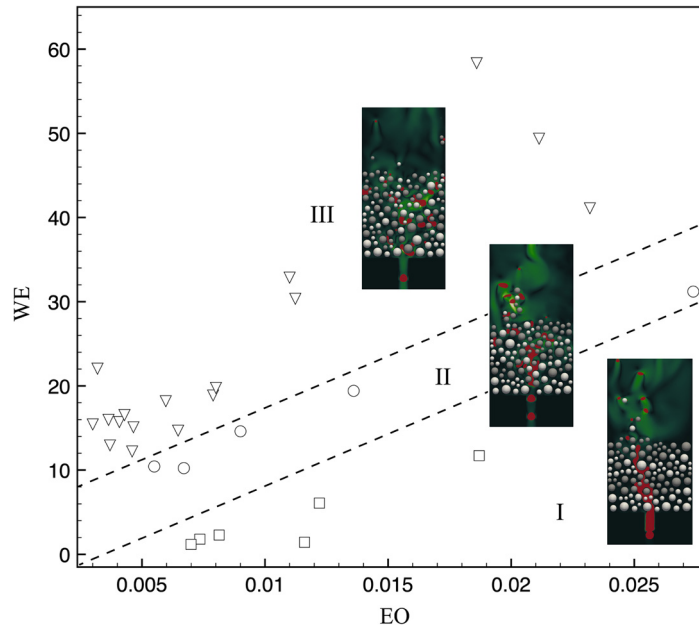


Fig. 24. Flow regimes of rising bubbles in sediment. The different regions are connected finger flow (square, Region I), transition flow (circle, Region II), and dispersed bubble flow (triangle, Region III). The dashed line indicates the transition boundary.

$$WE = \frac{\rho \bar{v}^2 L}{\sigma}, \quad (73)$$

where  $\bar{v}$  is the averaged velocity of the gas phase. We run 28 simulations by adjusting the IFT ranged from 0.01 to 0.07 and leak flow velocity ranged from 0.01 m/s to 0.1 m/s. The resulted EO and WE numbers for each case are plotted in Fig. 24.

Three typical flow regimes of bubble rising in sediment can be identified in our simulation results, namely, connected finger flow (Region I), transition flow (Region II), dispersed bubble flow (Region III). In region I, the IFT is high, and the kinetic energy of the gas phase is low. Therefore, the leaked bubbles coalesced and formed a connected plume. The inertia of gas is not sufficient to rupture the interface of the plume. The surface tension energy dominates in this region, and the momentum of bubbles is too low to displace the particles. Therefore, the pore spaces remain in their original configurations, and the behavior of connected finger flow is similar to that in the consolidated sediment system (central plume under low IFT condition). On the other hand, the leaked gas breaks into small bubbles and forms dispersed bubbly flow in Region III. In region III, the bubbles highly interact with the particles (high momentum exchange) due to the increasing kinetic energy of the gas phase. Small bubbles occupy the constantly changing pore spaces with a relatively uniform size distribution (Fig. 24). The bubbles widely spread over the domain, and the area of bubble dispersion in the pure liquid region is large.

The original sediment layer structure is destroyed due to the dispersed bubbly flow. Besides, significant instability of the rising paths can be observed. The particles are in a chaotic state, and their trajectories show random characteristics. In Region II, the bubble plume is partially discontinuous, and an uneven distribution of bubbles along the vertical direction is observed, which can be identified as the transition from connected finger flow to dispersed bubble flow. The particles are partially displaced due to the increasing momentum transfer between particles and fluids. The connected gas cluster and the disconnected bubbles coexist in the pore spaces of the sediment in Region II. It is worth noting that the transition line (dashed line in Fig. 24) between dispersed bubble flow and transition flow is almost parallel to the transition line between connected finger flow and transition flow. The gentle slope of the transition line indicates that the buoyancy force has less contribution to determining the flow behavior than the capillary force and the inertial force. These transition lines may vary depending on the particle-fluid density ratio, fluid viscosity ratio, and the sediment's confining pressure.

#### 4. Conclusion

This paper proposes a numerical model for simulating the solid-liquid-gas three-phase flow in unconsolidated particle layers. This model is developed based on the two-way coupling of the DEM for grains and the LBM multiphase algorithm for fluids. In this model, the fluid-fluid interface is treated by solving the mass transport using a phase-field method, and the multiphase fluid-particle interaction is tackled by a combination of the momentum exchange method for the flow field and the IBM for the phase field. The IBM for the zero-flux condition is adopted to treat the moving particles' boundary in the phase field. Such solution prevents the penetration of fluid-fluid interface into the grains and ensures the mass conservation of each fluid phase. In addition, the implementation of our method is simple and most calculations are local, making the parallelization of the code easy and natural. Our method successfully captures the complex phenomena in gas bubble coalescence or breakup and the interaction of multiphase interfaces with solid particles.

We applied the method to simulate the process of upward migration of leaked gas bubbles through a brine-filled sediment column at the seafloor and elucidate the influences of leak flow rate and interfacial tension on the phenomena. The dimensionless EO and WE numbers can identify the three different flow regimes (connected finger flow, transition flow, dispersed bubbly flow). It is found that the surface tension force and the buoyancy force play a major role in determining the flow behavior. The proposed numerical method has powerful advantages in simulating such complex fluid-solid coupling problems, especially when the multiphase fluid-solid interactions at the mesoscale (grain scale) are important.

#### CRediT authorship contribution statement

**Fei Jiang:** Conceptualization, Investigation, Methodology, Software, Validation, Writing – original draft. **Haihu Liu:** Investigation, Methodology. **Xian Chen:** Writing – review & editing. **Takeshi Tsuji:** Writing – review & editing.

#### Declaration of competing interest

The authors declare that they have no known competing financial interests or personal relationships that could have appeared to influence the work reported in this paper.

#### Acknowledgements

This work is supported by JSPS through a Grant-in-Aid for Young Scientists (19K15100). This work is also partially supported by the National Natural Science Foundation of China (Grant Nos. 12072257, 51876170), the National Key Project (Grant No. GJXM92579), and the Natural Science Basic Research Plan in Shaanxi Province of China (Grant No. 2019JM-343).

#### Appendix A. Transformation matrix of MRT model

The transformation matrix  $M$  in MRT model is given as

$$M = \begin{bmatrix} 1 & 1 & 1 & 1 & 1 & 1 & 1 & 1 & 1 \\ -4 & -1 & -1 & -1 & -1 & 2 & 2 & 2 & 2 \\ 4 & -2 & -2 & -2 & -2 & 1 & 1 & 1 & 1 \\ 0 & 1 & 0 & -1 & 0 & 1 & -1 & -1 & 1 \\ 0 & -2 & 0 & 2 & 0 & 1 & -1 & -1 & 1 \\ 0 & 0 & 1 & 0 & -1 & 1 & 1 & -1 & -1 \\ 0 & 0 & -2 & 0 & 2 & 1 & 1 & -1 & -1 \\ 0 & 1 & -1 & 1 & -1 & 0 & 0 & 0 & 0 \\ 0 & 0 & 0 & 0 & 0 & 1 & -1 & 1 & -1 \end{bmatrix} \quad (74)$$

## Appendix B. Implementation of the recoloring algorithm

The recoloring algorithm is adopted to achieve the separation of the two fluids. The recolor algorithm must conserve both the masses of the two fluids and the momentum of the mixture, which is implemented as follow [39]:

---

### Algorithm 1 Recoloring algorithm.

---

```

for  $a = 1, 17, 2$  do
   $sp = e[a] \cdot C_g$ 
   $tmp = sp * (1/|C_g|) * \min(g^b[a], g^b[a+1], g^r[a], g^r[a+1])$ 
   $g^r[a] = g^r[a] + tmp$ 
   $g^r[a+1] = g^r[a+1] - tmp$ 
   $g^b[a] = g^b[a] - tmp$ 
   $g^b[a+1] = g^b[a+1] + tmp$ 
end for

```

---

Note that the above algorithm requires the lattice vectors to be sorted in antiparallel pairs.

## References

- [1] Fumio Inagaki, K.-U. Hinrichs, Yusuke Kubo, Marshall W. Bowles, Verena B. Heuer, W.-L. Hong, Tatsuhiko Hoshino, Akira Ijiri, Hiroyuki Imachi, Motoo Ito, et al., Exploring deep microbial life in coal-bearing sediment down to - 2.5 km below the ocean floor, *Science* 349 (6246) (2015) 420–424.
- [2] K. Stratford, R. Adhikari, Ignacio Pagonabarraga, J.-C. Desplat, Lattice Boltzmann for binary fluids with suspended colloids, *J. Stat. Phys.* 121 (1) (2005) 163–178.
- [3] Kevin Stratford, Ronjooy Adhikari, Ignacio Pagonabarraga, J.-C. Desplat, Michael E. Cates, Colloidal jamming at interfaces: a route to fluid-bicontinuous gels, *Science* 309 (5744) (2005) 2198–2201.
- [4] Fabian Jansen, Jens Harting, From bijels to pickering emulsions: a lattice Boltzmann study, *Phys. Rev. E* 83 (4) (2011) 046707.
- [5] D.F. Boutt, B.K. Cook, J.R. Williams, A coupled fluid–solid model for problems in geomechanics: application to sand production, *Int. J. Numer. Anal. Methods Geomech.* 35 (9) (2011) 997–1018.
- [6] Zhengbiao Peng, Elham Doroodchi, Caimao Luo, Behdad Moghtaderi, Influence of void fraction calculation on fidelity of CFD-DEM simulation of gas–solid bubbling fluidized beds, *AIChE J.* 60 (6) (2014) 2000–2018.
- [7] K.W. Chu, Bo Wang, A.B. Yu, Andrew Vince, CFD-DEM modelling of multiphase flow in dense medium cyclones, *Powder Technol.* 193 (3) (2009) 235–247.
- [8] H. Kruggel-Emden, B. Kravets, M.K. Suryanarayana, R. Jasevicius, Direct numerical simulation of coupled fluid flow and heat transfer for single particles and particle packings by a LBM-approach, *Powder Technol.* 294 (2016) 236–251.
- [9] Zhipeng Qin, Jenny Suckale, Direct numerical simulations of gas–solid–liquid interactions in dilute fluids, *Int. J. Multiph. Flow* 96 (2017) 34–47.
- [10] M.W. Baltussen, Luuk J.H. Seelen, J.A.M. Kuipers, N.G. Deen, Direct numerical simulations of gas–liquid–solid three phase flows, *Chem. Eng. Sci.* 100 (2013) 293–299.
- [11] Y. Li, G.Q. Yang, J.P. Zhang, L.-S. Fan, Numerical studies of bubble formation dynamics in gas–liquid–solid fluidization at high pressures, *Powder Technol.* 116 (2–3) (2001) 246–260.
- [12] Yang Ge, Liang-Shih Fan, 3-D direct numerical simulation of gas–liquid and gas–liquid–solid flow systems using the level-set and immersed-boundary methods, *Adv. Chem. Eng.* 31 (2006) 1–63.
- [13] Deepak Jain, Niels G. Deen, J.A.M. Kuipers, Sergiy Antonyuk, Stefan Heinrich, Direct numerical simulation of particle impact on thin liquid films using a combined volume of fluid and immersed boundary method, *Chem. Eng. Sci.* 69 (1) (2012) 530–540.
- [14] Zhe Li, Julien Favier, Umberto D’Ortona, Sébastien Poncet, An immersed boundary-lattice Boltzmann method for single-and multi-component fluid flows, *J. Comput. Phys.* 304 (2016) 424–440.
- [15] Yu Chen, Qunjun Kang, Qingdong Cai, Moran Wang, Dongxiao Zhang, Lattice Boltzmann simulation of particle motion in binary immiscible fluids, *Commun. Comput. Phys.* 18 (3) (2015) 757–786.
- [16] Mark Sussman, Elbridge Gerry Puckett, A coupled level set and volume-of-fluid method for computing 3d and axisymmetric incompressible two-phase flows, *J. Comput. Phys.* 162 (2) (2000) 301–337.
- [17] Fei Jiang, Kazuki Matsumura, Junji Ohgi, Xian Chen, A GPU-accelerated fluid–structure-interaction solver developed by coupling finite element and lattice Boltzmann methods, *Comput. Phys. Commun.* (2020) 107661.
- [18] Fei Jiang, Takeshi Tsuji, Impact of interfacial tension on residual CO<sub>2</sub> clusters in porous sandstone, *Water Resour. Res.* 51 (3) (2015) 1710–1722.
- [19] Fei Jiang, Takeshi Tsuji, Numerical investigations on the effect of initial state CO<sub>2</sub> topology on capillary trapping efficiency, *Int. J. Greenh. Gas Control* 49 (2016) 179–191.
- [20] F. Jiang, T. Tsuji, Estimation of three-phase relative permeability by simulating fluid dynamics directly on rock-microstructure images, *Water Resour. Res.* 53 (1) (2017) 11–32.
- [21] Haihu Liu, Yang Lu, Sheng Li, Yuan Yu, Kirti Chandra Sahu, Deformation and breakup of a compound droplet in three-dimensional oscillatory shear flow, *Int. J. Multiph. Flow* (2020) 103472.
- [22] Peter A. Cundall, Otto D.L. Strack, A discrete numerical model for granular assemblies, *Geotechnique* 29 (1) (1979) 47–65.
- [23] Xiaosong Sun, Mikio Sakai, Three-dimensional simulation of gas–solid–liquid flows using the DEM-VOF method, *Chem. Eng. Sci.* 134 (2015) 531–548.
- [24] Shuo Li, Shintaro Kajiwara, Mikio Sakai, Numerical investigation on the mixing mechanism in a cross-torus paddle mixer using the DEM-CFD method, *Powder Technol.* (2020).
- [25] Y.T. Feng, K. Han, D.R.J. Owen, Coupled lattice Boltzmann method and discrete element modelling of particle transport in turbulent fluid flows: computational issues, *Int. J. Numer. Methods Eng.* 72 (9) (2007) 1111–1134.
- [26] Min Wang, Y.T. Feng, D.R.J. Owen, T.M. Qu, A novel algorithm of immersed moving boundary scheme for fluid–particle interactions in DEM-LBM, *Comput. Methods Appl. Mech. Eng.* 346 (2019) 109–125.
- [27] G.C. Yang, L. Jing, C.Y. Kwok, Y.D. Sobral, A comprehensive parametric study of LBM-DEM for immersed granular flows, *Comput. Geotech.* 114 (2019) 103100.
- [28] Franck Lominé, Luc Scholtes, Luc Sibille, Philippe Poullain, Modeling of fluid–solid interaction in granular media with coupled lattice Boltzmann/discrete element methods: application to piping erosion, *Int. J. Numer. Anal. Methods Geomech.* 37 (6) (2013) 577–596.

- [29] Xilin Cui, Jun Li, Andrew Chan, David Chapman, Coupled DEM–LBM simulation of internal fluidisation induced by a leaking pipe, *Powder Technol.* 254 (2014) 299–306.
- [30] D.R.J. Owen, C.R. Leonardi, Y.T. Feng, An efficient framework for fluid–structure interaction using the lattice Boltzmann method and immersed moving boundaries, *Int. J. Numer. Methods Eng.* 87 (1–5) (2011) 66–95.
- [31] Alessandro Leonardi, Falk K. Wittel, Miller Mendoza, Hans J. Herrmann, Coupled DEM–LBM method for the free-surface simulation of heterogeneous suspensions, *Comput. Part. Mech.* 1 (1) (2014) 3–13.
- [32] Mouloud Mansouri, Moulay Saïd El Youssofi, François Nicot, Numerical simulation of the quicksand phenomenon by a 3d coupled discrete element-lattice Boltzmann hydromechanical model, *Int. J. Numer. Anal. Methods Geomech.* 41 (3) (2017) 338–358.
- [33] D.R. Noble, J.R. Torczynski, A lattice-Boltzmann method for partially saturated computational cells, *Int. J. Mod. Phys. C* 9 (08) (1998) 1189–1201.
- [34] Kosuke Suzuki, Takaji Inamuro, Effect of internal mass in the simulation of a moving body by the immersed boundary method, *Comput. Fluids* 49 (1) (2011) 173–187.
- [35] Anthony J.C. Ladd, Numerical simulations of particulate suspensions via a discretized Boltzmann equation. Part 1. Theoretical foundation, *J. Fluid Mech.* 271 (1994) 285–309.
- [36] Cyrus K. Aidun, Yunnan Lu, E. Ding, et al., Direct analysis of particulate suspensions with inertia using the discrete Boltzmann equation, 1998.
- [37] Wen-Tao Ding, Wen-Jie Xu, Study on the multiphase fluid-solid interaction in granular materials based on an LBM–DEM coupled method, *Powder Technol.* 335 (2018) 301–314.
- [38] Yuki Kano, Toru Sato, Hiroyuki Oyama, Numerical study on the formations of gas channels and subsequent bubbles in unconsolidated sandy seabed sediment using a coupled LBM–DEM method, *J. Nat. Gas Sci. Eng.* 74 (2020) 103101.
- [39] Jonas Tölke, Lattice Boltzmann simulations of binary fluid flow through porous media, *Philos. Trans. R. Soc. Lond. A, Math. Phys. Eng. Sci.* 360 (1792) (2002) 535–545.
- [40] Fei Jiang, Takeshi Tsuji, Changhong Hu, Elucidating the role of interfacial tension for hydrological properties of two-phase flow in natural sandstone by an improved lattice Boltzmann method, *Transp. Porous Media* 104 (1) (2014) 205–229.
- [41] Haihu Liu, Albert J. Valocchi, Yonghao Zhang, Qinqun Kang, Lattice Boltzmann phase-field modeling of thermocapillary flows in a confined microchannel, *J. Comput. Phys.* 256 (2014) 334–356.
- [42] Haihu Liu, Lei Wu, Yan Ba, Guang Xi, Yonghao Zhang, A lattice Boltzmann method for axisymmetric multicomponent flows with high viscosity ratio, *J. Comput. Phys.* 327 (2016) 873–893.
- [43] Pierre Lallemand, Li-Shi Luo, Theory of the lattice Boltzmann method: dispersion, dissipation, isotropy, galilean invariance, and stability, *Phys. Rev. E* 61 (6) (2000) 6546.
- [44] Haihu Liu, Albert J. Valocchi, Qinqun Kang, Three-dimensional lattice Boltzmann model for immiscible two-phase flow simulations, *Phys. Rev. E* 85 (4) (2012) 046309.
- [45] M’hamed Bouzidi, Mouaouia Firdaouss, Pierre Lallemand, Momentum transfer of a Boltzmann-lattice fluid with boundaries, *Phys. Fluids* 13 (11) (2001) 3452–3459.
- [46] Pierre Lallemand, Li-Shi Luo, Lattice Boltzmann method for moving boundaries, *J. Comput. Phys.* 184 (2) (2003) 406–421.
- [47] Kosuke Suzuki, Tsuyoshi Kawasaki, Naoki Furumachi, Youming Tai, Masato Yoshino, A thermal immersed boundary–lattice Boltzmann method for moving-boundary flows with Dirichlet and Neumann conditions, *Int. J. Heat Mass Transf.* 121 (2018) 1099–1117.
- [48] Zhaoli Guo, Chang Shu, *Lattice Boltzmann Method and Its Applications in Engineering*, vol. 3, World Scientific, 2013.
- [49] Paul J. Dellar, Incompressible limits of lattice Boltzmann equations using multiple relaxation times, *J. Comput. Phys.* 190 (2) (2003) 351–370.
- [50] Shiyi Chen, Gary D. Doolen, Lattice Boltzmann method for fluid flows, *Annu. Rev. Fluid Mech.* 30 (1) (1998) 329–364.
- [51] Dominique d’Humières, Multiple-relaxation-time lattice Boltzmann models in three dimensions, *Philos. Trans. R. Soc. Lond. A, Math. Phys. Eng. Sci.* 360 (1792) (2002) 437–451.
- [52] Irina Ginzburg, Variably saturated flow described with the anisotropic lattice Boltzmann methods, *Comput. Fluids* 35 (8–9) (2006) 831–848.
- [53] Zhaoli Guo, Chuguang Zheng, Analysis of lattice Boltzmann equation for microscale gas flows: relaxation times, boundary conditions and the Knudsen layer, *Int. J. Comput. Fluid Dyn.* 22 (7) (2008) 465–473.
- [54] Jeremiah U. Brackbill, Douglas B. Kothe, Charles Zemach, A continuum method for modeling surface tension, *J. Comput. Phys.* 100 (2) (1992) 335–354.
- [55] Yu Chen, Albert J. Valocchi, Qinqun Kang, Hari S. Viswanathan, Inertial effects during the process of supercritical CO<sub>2</sub> displacing brine in a sandstone: lattice Boltzmann simulations based on the continuum-surface-force and geometrical wetting models, *Water Resour. Res.* 55 (12) (2019) 11144–11165.
- [56] M. Latva-Kokko, Daniel H. Rothman, Static contact angle in lattice Boltzmann models of immiscible fluids, *Phys. Rev. E* 72 (4) (2005) 046701.
- [57] Sébastien Leclaire, Kamelia Abahri, Rafik Belarbi, Rachid Bennacer, Modeling of static contact angles with curved boundaries using a multiphase lattice Boltzmann method with variable density and viscosity ratios, *Int. J. Numer. Methods Fluids* 82 (8) (2016) 451–470.
- [58] Abbas Fakhari, Diogo Bolster, Diffuse interface modeling of three-phase contact line dynamics on curved boundaries: a lattice Boltzmann model for large density and viscosity ratios, *J. Comput. Phys.* 334 (2017) 620–638.
- [59] Sheng Li, Yang Lu, Fei Jiang, Haihu Liu, Lattice Boltzmann simulation of three-phase flows with moving contact lines on curved surfaces, *Phys. Rev. E* 104 (Jul 2021) 015310.
- [60] H.L. Wang, Z.H. Chai, B.C. Shi, H. Liang, Comparative study of the lattice Boltzmann models for Allen-Cahn and Cahn-Hilliard equations, *Phys. Rev. E* 94 (3) (2016) 033304.
- [61] Haibo Huang, Hongwei Zheng, Xi-yun Lu, Chang Shu, An evaluation of a 3d free-energy-based lattice Boltzmann model for multiphase flows with large density ratio, *Int. J. Numer. Methods Fluids* 63 (10) (2010) 1193–1207.
- [62] Pengtao Yue, Chunfeng Zhou, James J. Feng, Spontaneous shrinkage of drops and mass conservation in phase-field simulations, *J. Comput. Phys.* 223 (1) (2007) 1–9.
- [63] Lin Zheng, Taehun Lee, Zhaoli Guo, David Rumschitzki, Shrinkage of bubbles and drops in the lattice Boltzmann equation method for nonideal gases, *Phys. Rev. E* 89 (3) (2014) 033302.
- [64] Abbas Fakhari, Martin Geier, Taehun Lee, A mass-conserving lattice Boltzmann method with dynamic grid refinement for immiscible two-phase flows, *J. Comput. Phys.* 315 (2016) 434–457.
- [65] Xiao-Dong Niu, You Li, Yi-Ren Ma, Mu-Feng Chen, Xiang Li, Qiao-Zhong Li, A mass-conserving multiphase lattice Boltzmann model for simulation of multiphase flows, *Phys. Fluids* 30 (1) (2018) 013302.
- [66] Fuminori Horai, Takahiro Nakagami, Takaji Inamuro, A study of conservative diffuse-interface models of an improved two-phase lattice Boltzmann method, in: *Proceedings of the 32nd Symposium on Computational Fluid Dynamics*, 2018, pp. F09–3.
- [67] Jonas Tölke, Sören Freudiger, Manfred Krafczyk, An adaptive scheme using hierarchical grids for lattice Boltzmann multi-phase flow simulations, *Comput. Fluids* 35 (8–9) (2006) 820–830.
- [68] Marc André Meyers, Krishan Kumar Chawla, *Mechanical Behavior of Materials*, Cambridge University Press, 2008.
- [69] Christian Labra, *Advances in the development of the discrete element method for excavation processes*, PhD thesis, Universitat Politècnica de Catalunya, Barcelona, 2012.
- [70] M.B.B.J.M. Tuckerman, Bruce J. Berne, Glenn J. Martyna, Reversible multiple time scale molecular dynamics, *J. Chem. Phys.* 97 (3) (1992) 1990–2001.
- [71] Richard J. Bathurst, Leo Rothenburg, *Micromechanical Aspects of Isotropic Granular Assemblies with Linear Contact Interactions*, 1988.

- [72] Sébastien Hentz, Frédéric V. Donzé, Laurent Daudeville, Discrete element modelling of concrete submitted to dynamic loading at high strain rates, *Comput. Struct.* 82 (29–30) (2004) 2509–2524.
- [73] Kendall E. Atkinson, *An Introduction to Numerical Analysis*, John Wiley & Sons, 2008.
- [74] P.-H. Kao, R.-J. Yang, An investigation into curved and moving boundary treatments in the lattice Boltzmann method, *J. Comput. Phys.* 227 (11) (2008) 5671–5690.
- [75] Li Chen, Yang Yu, Jianhua Lu, Guoxiang Hou, A comparative study of lattice Boltzmann methods using bounce-back schemes and immersed boundary ones for flow acoustic problems, *Int. J. Numer. Methods Fluids* 74 (6) (2014) 439–467.
- [76] Xuhui Li, Fei Jiang, Changhong Hu, Analysis of the accuracy and pressure oscillation of the lattice Boltzmann method for fluid–solid interactions, *Comput. Fluids* 129 (2016) 33–52.
- [77] A. Caiazzo, Analysis of lattice Boltzmann nodes initialisation in moving boundary problems, *Prog. Comput. Fluid Dyn.* 8 (1–4) (2008) 3–10.
- [78] Giacomo Falcucci, Matteo Aureli, Stefano Ubertini, Maurizio Porfiri, Transverse harmonic oscillations of laminae in viscous fluids: a lattice Boltzmann study, *Philos. Trans. R. Soc. A, Math. Phys. Eng. Sci.* 369 (1945) (2011) 2456–2466.
- [79] Alessandro De Rosi, Stefano Ubertini, Francesco Ubertini, A comparison between the interpolated bounce-back scheme and the immersed boundary method to treat solid boundary conditions for laminar flows in the lattice Boltzmann framework, *J. Sci. Comput.* 61 (3) (2014) 477–489.
- [80] Takaji Inamuro, Koji Maeba, Fumimaru Ogino, Flow between parallel walls containing the lines of neutrally buoyant circular cylinders, *Int. J. Multiph. Flow* 26 (12) (2000) 1981–2004.
- [81] Fei Jiang, Kangping Liao, Kazuki Matsumura, Junji Ohgi, Xian Chen, Simulation of fluid–structure interaction problems with thin elastic plate via the coupling of finite element and lattice Boltzmann methods, *Int. J. Comput. Methods* (2020) 2050013.
- [82] Charles S. Peskin, The immersed boundary method, *Acta Numer.* 11 (2002) 479–517.
- [83] Xitong Zhang, Haihu Liu, Jinggang Zhang, A new capillary force model implemented in lattice Boltzmann method for gas–liquid–solid three-phase flows, *Phys. Fluids* 32 (10) (2020) 103301.
- [84] Julian A. Simeonov, Joseph Calantoni, Modeling mechanical contact and lubrication in direct numerical simulations of colliding particles, *Int. J. Multiph. Flow* 46 (2012) 38–53.
- [85] N.-Q. Nguyen, A.J.C. Ladd, Lubrication corrections for lattice-Boltzmann simulations of particle suspensions, *Phys. Rev. E* 66 (4) (2002) 046708.
- [86] R. Hart, Peter A. Cundall, J. Lemos, Formulation of a three-dimensional distinct element model-part. II. Mechanical calculations for motion and interaction of a system composed of many polyhedral blocks, *Int. J. Rock Mech. Min. Sci. Geomech. Abstr.* 25 (1988) 117–125.
- [87] Haihu Liu, Yonghao Zhang, Lattice Boltzmann simulation of the trapping of a microdroplet in a well of surface energy, *Comput. Fluids* 155 (2017) 68–75.
- [88] Isolde B. Belien, Katharine V. Cashman, Alan W. Rempel, Gas accumulation in particle-rich suspensions and implications for bubble populations in crystal-rich magma, *Earth Planet. Sci. Lett.* 297 (1–2) (2010) 133–140.
- [89] Qisu Zou, Xiaoyi He, On pressure and velocity boundary conditions for the lattice Boltzmann BGK model, *Phys. Fluids* 9 (6) (1997) 1591–1598.
- [90] Guo Zhao-Li, Zheng Chu-Guang, Shi Bao-Chang, Non-equilibrium extrapolation method for velocity and pressure boundary conditions in the lattice Boltzmann method, *Chin. Phys.* 11 (4) (2002) 366.
- [91] Haibo Huang, Jun-Jie Huang, Xi-Yun Lu, Michael C. Sukop, On simulations of high-density ratio flows using color-gradient multiphase lattice Boltzmann models, *Int. J. Mod. Phys. C* 24 (04) (2013) 1350021.
- [92] Takeshi Tsuji, Fei Jiang, Kenneth T. Christensen, Characterization of immiscible fluid displacement processes with various capillary numbers and viscosity ratios in 3d natural sandstone, *Adv. Water Resour.* 95 (2016) 3–15.
- [93] Roland Clift, John R. Grace, Martin E. Weber, *Bubbles, Drops, and Particles*, Courier Corporation, 2005.
- [94] Liang Hu, Mingbo Li, Wenyu Chen, Haibo Xie, Xin Fu, Bubbling behaviors induced by gas-liquid mixture permeating through a porous medium, *Phys. Fluids* 28 (8) (2016) 087102.